Density Tapering for Sparse Planar Spiral Antenna Arrays

J.G.M. Keijsers

Delft University of Technology

TU Delft Delft University of Technology

Challenge the future

Density Tapering for Sparse Planar Spiral Antenna Arrays

by

J.G.M. Keijsers

to obtain the degree of Master of Science
in Electrical Engineering - *Telecommunications & Sensing Systems*
at the Delft University of Technology,
to be defended publicly on Friday October 21, 2016 at 10:00 AM.

Student number:	4087313	
Thesis committee:	Prof. DSc. A. Yarovoy,	TU Delft, supervisor
	Dr. Ir. B. J. Kooij,	TU Delft
	Prof. Dr. H.H.F. Jos,	Chalmers University of Technology

TU Delft

ABSTRACT

Increasing demands for mobile internet access have led to exponential developments in mobile communications technologies. The next generation mobile technology is expected to exploit electronic beam steering and to have a higher operating frequency to facilitate a higher bandwidth. This places a heavy burden on the base station antenna arrays, which should be sparse to accommodate passively cooling the system.

Conventional sparse array topologies suffer from undesirable radiation pattern characteristics such as grating lobes. Therefore, this work focused on exploring methods to synthesize the antenna elements' geometrical parameters to enhance the radiation pattern and to explore the limitations that arise due to the array's sparseness. To this end, both a deterministic and a stochastic method were proposed.

Starting with an analytical window function as a continuous current distribution and approximating this by adjusting the antenna elements' radial coordinates results in the fact that the desired window's radiation pattern is only approximated in a limited field of view, depending on the sparseness. Full electromagnetic wave simulations are performed to show that downscaling the topology to make it more dense gives rise to increased coupling effects that deteriorate the array's performance.

In addition to the deterministic method, a genetic algorithm optimization method is employed to stochastically obtain the optimal current distribution window. Approximating the optimal continuous current distribution again leads to the array factor following the optimal window's radiation pattern in a limited field of view.

Furthermore, it is shown that for the conditions used in this work, the optimum continuous current distribution is also the optimum current distribution for finite element arrays, implying that only one optimization needs to be executed when designing such an array.

Concluding, the applicability of density tapering to sparse arrays is limited. The inherent undersampling causes a limited realization of the window function's characteristics. Density tapering does improve the absolute performance of a sparse array in terms of peak sidelobe level, but may be useful if the region of interest is concentrated near the main beam. The requirements and in particular the region of interest of the application determine whether density tapering can be effectively employed.

PREFACE

Before you lies my master thesis report, which is the final part of my Master of Science in Electrical Engineering at Delft University of Technology. This work has been executed at the Microwave Sensing, Signals and Systems (MS3) group at the faculty of Electrical Engineering, Mathematics and Computer Science (EEMCS). It describes the research I carried out for Ampleon, to explore the possibilities for sparse antenna arrays, aimed at the next generation mobile communication base stations. The project was supervised by Prof. DSc. Yarovoy of Delft University of Technology and Prof. Dr. Jos of Ampleon.

Over the course of this project, I have learned many things, mainly about shaping and planning an initially unclear objective. Working individually for such a period of time has taught me discipline and forced me to employ creativity in order to contribute to the scientific community in a novel way. In the end, I believe I have found novelty amongst the already extensive research on antenna arrays by exploring the applicability of density tapering methods to sparse spiral antenna arrays. With this, I believe this report is a fitting final chapter to my career at TU Delft.

I want to express my gratitude to everyone involved in supporting me. Firstly, Alexander Yarovoy for his sincere support, extensive knowledge and guidance during the project. On behalf of Ampleon, I want to thank Rik Jos and Sergio Pires for supplying the framework of the project, providing a pleasant positive feedback atmosphere and keeping an open mind throughout the project while keeping the project relevant for all parties involved. Also, my gratitude goes out to Antoine Roederer for his knowledgeable advise, open-minded insights and off the beaten path suggestions. Closely related, I would like to thank the entire MS3 group, staff and particularly the other master students for providing a stimulating, relaxed atmosphere where anyone would feel welcome and comfortable.

Lastly, I would like to express my gratitude to my friends and family for supporting me each in their own way during this project and really throughout my whole studies and life.

J.G.M. Keijsers
Delft, September 2016

Contents

List of Figures

1

INTRODUCTION & MOTIVATION

The ever-increasing demand for more and faster mobile internet access has led to exponential developments in mobile communication technology. In 1999, people on the street said they thought that having a mobile phone was ridiculous, whereas now, life without one is unimaginable to most people. At the moment, there are 7.3 billion mobile subscriptions in the world, more than the number of people on the planet [1]. With the rapid development of the internet of things, it is expected that by 2021, there will be over 9 billion mobile subscriptions [1]. Specifically, the total mobile data traffic is expected to rise from 120 exabyte[1] in the last five years to 1600 exabyte by 2021, a factor 13 increase [1].

Globally, this drastic need for speed has triggered researchers and scientists to explore ideas in relation to increasing the bandwidth of the channel, which is related to the maximum rate of information transfer by the well-known Shannon-Hartley theorem:

$$C = B \log_2(1 + \frac{S}{N}) \tag{1.1}$$

where C is the channel capacity, B is the bandwidth of the channel and $\frac{S}{N}$ is the signal-to-noise ratio. The relation between bandwidth and capacity is not completely linear, as the signal-to-noise ratio also depends on the bandwidth. Also, this theorem relies on assumptions of the channel and noise that are not valid for real life mobile communications, but it serves as a base to illustrate the positive relation between bandwidth and channel capacity.

Current mobile technologies, GSM, UMTS and LTE, have an operating frequency of up to 2.6 GHz. To increase the bandwidth, the operating frequency of the next generation mobile communications is expected to increase: a relative bandwidth of 10% will result in 300 MHz at 3 GHz, while a 3 GHz bandwidth is achieved at an operating frequency of 30 GHz. The opportunities for increasing the information transfer rate by increasing the operating frequency are evident.

In addition, spatial diversity will be employed in order to re-use the same channels for multiple users. As illustrated in Figure 1.1, current technologies typically employ slightly directive antennas to divide cells in three sectors. Figure 1.2 illustrates the use of beam steering to exploit the spatial diversity of different users. Beam steering allows the same resources to be used for different users. In the displayed situation, the antenna array will need to be able to steer its beam from $-45°$ to $+45°$ in one plane.

It is noted that the specifications for the next mobile communication technology are not yet definite, so this work will strive to be applicable in general. Since the system level specifications are not yet determined, in this work it is supposed that the requirements are to scan in elevation up to 45° for all azimuthal directions and the operating frequency will be 30 GHz.

In antenna theory, most rules are based on the length in terms of the wavelength λ, which is known as the electrical length. As the operational frequency increases, the wavelength decreases. The structures and rules are still valid in terms of electrical length, but the physical dimensions decrease. However, the circuitry behind the antennas, such as amplifiers and phase shifters, does not scale with frequency in the same way. As a result, the circuitry would be very closely placed together in conventional antenna array designs, thus resulting in an inability to dissipate the heat formed by thermal dissipation. Furthermore, in general, the higher the frequency, the lower the efficiency of the circuitry will be, which leads to even more heat development.

[1] 1 exabyte = 1 billion gigabyte

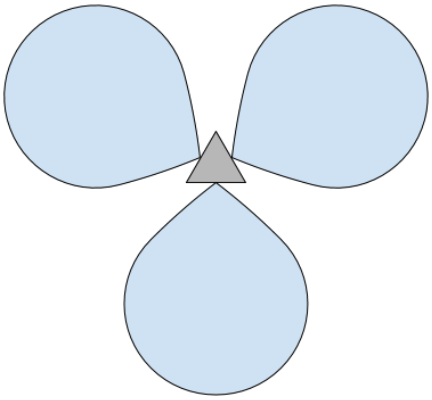

Figure 1.1: Typical sectorization as used in mobile communication technologies up to 4G.

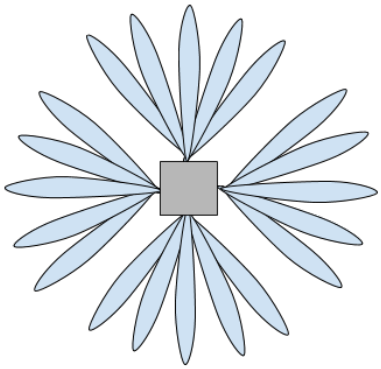

Figure 1.2: Possible sectorization as to be used in the next mobile communication technology.

For this reason, this work will focus on ways of placing antenna elements in an array sufficiently well spaced apart for the heat to be dissipated passively, without any significant degradation in performance. It is estimated that a minimum spacing of 1.1λ between the elements is required in order to passively cool the system. This work will examine techniques that may be used to minimize the performance degradation for sparse arrays.

1.1. PROBLEM FORMULATION

For the fundamentals of antenna array theory, the reader is referred to the standard literature such as Chapter 6 from Balanis [2] or Chapter 3 from Milligan [3].

For an antenna array consisting of N elements located at positions $\boldsymbol{r}_n = (x_n, y_n, z_n),\ n = 1, \ldots, N$, the array factor can be expressed as [4]:

$$AF(\theta,\phi) = \sum_{n=1}^{N} w_n e^{-jk\boldsymbol{r}_n \cdot \hat{\boldsymbol{a}}(\theta,\phi)} \tag{1.2}$$

where $w_n = a_n e^{j\varphi_n}$ is the complex excitation coefficient consisting of amplitude a_n and phase φ_n of antenna element n, $k = 2\pi/\lambda$ is the wave number and $\hat{\boldsymbol{a}}(\theta,\phi) = \sin\theta\cos\phi\hat{\boldsymbol{x}} + \sin\theta\sin\phi\hat{\boldsymbol{y}} + \cos\theta\hat{\boldsymbol{z}}$ is the unit vector describing the far-field radiation direction. The radiation pattern of the antenna array depends on the array's geometrical ($\boldsymbol{r}_n$) and electrical (a_n, φ_n) parameters, as well as on the radiation pattern of each antenna element, $f_n(\theta,\phi)$, which may differ for each element because of mutual coupling effects. Neglecting these effects is often done as a first approximation to avoid the need for full-wave simulations. The product of the element pattern and the array factor can then be used as an approximation of the actual antenna array's radiation pattern:

$$E(\theta,\phi) \approx f_n(\theta,\phi) AF(\theta,\phi) \tag{1.3}$$

With this approximation, array design can be performed by focusing on the synthesis of the array factor $AF(\theta,\phi)$ without the necessity to select radiation elements yet. Thus, the focus lies on the array factor, such that the results are more generally applicable, and the choice of antenna element is left to the designer.

It is evident from Equation 1.2 that the influence of the antenna elements' positions on the array factor is highly non-linear, since $\boldsymbol{r}_n$ is in the exponent. Therefore, effective synthesis methods are not trivial, and so there is no one approach that always works. Only arrays placed on regular lattices have a nice, clean closed-form expression for the array factor. The aim of antenna array design is to find the geometrical and electrical parameters so that the resulting radiation pattern satisfies the specifications.

One of the most important implications regarding conventional arrays is the conclusion that radiation maxima can occur in unwanted directions when the spacing between elements is too large. These maxima, which are called grating lobes, are the result of constructive interference in unwanted directions. Evidently, directing energy to unwanted directions is to be avoided. To prevent these grating lobes from occurring in regular square grid arrays, the maximum allowable distance between neighbouring elements is $\lambda/2$. If a larger

inter-element distance is required, grating lobes can be prevented by choosing a suitable array topology. In other words, the array's geometrical parameters $\boldsymbol{r}_n$ are chosen to influence the array factor to avoid the presence of grating lobes.

This opportunity becomes the focus of this thesis. This work will **explore the possibilities of modifying the geometrical parameters of the array to enhance its radiation pattern, and explore the limitations that may arise due to the sparseness of the array.**

Chapter 2 will cover the current state of the art of (sparse) antenna arrays as reported in the literature, in which Sections 2.2 and 2.3 will elaborate on ways to enhance the performance of such arrays, by means of density tapering and optimization. In this work, both methods will be employed. First, Chapter 3 examines density tapering as an analytical method to enhance the radiation pattern. Chapter 4 describes how an optimization approach is taken as an alternative to analytical density tapering. A full electromagnetic wave simulation is then done to see whether the proposed ideas hold in a realistic environment, which is reported on and analysed in Chapter 5. Finally, Chapter 6 contains the conclusions and recommendations for further work.

2

State of the Art

Although the concept stems back to the first half of the twentieth century [5], phased antenna arrays were not extensively used in the past due to the complexity of the feeding network and the implementation costs. However, the great technological advances of the last decades have made it possible to implement phased antenna arrays and to exploit their advantages such as a highly directive beam which can be scanned electronically [6]. As discussed in Section 1.1, the physical layout of the antenna array is vital to its performance. This section will therefore list some of the options for placing antenna elements in an array.

2.1. Base Array Topology

Placing antenna elements on a regular lattice is the most straightforward way of deploying antenna elements in an array. Such a geometry is convenient to manufacture and lends itself to exact mathematical analysis. While this geometry may be favourable in some applications due to its simplicity, its regularity means that grating lobes will appear when this structure is applied in a sparse array, where the distance between neighbouring elements exceeds half a wavelength [2]. An aperiodic structure is required to obtain a desirable radiation pattern.

Introducing some irregularity to the uniform lattice antenna array can be achieved simply by removing some of the elements. This process is called thinning [7–22]. Naturally, the question that follows is which elements should be removed from the grid and which should be kept. Ishimaru [7] proposed an analytical method to synthesize linear arrays and achieve a prespecified array factor. In this endeavour, an estimate of the maximum sidelobe level is formulated, which linearly decreases with the number of elements. Lockwood used sparse periodic linear [8] and two-dimensional [9] antenna arrays, and made use of the convolution effect present when using a different transmit and receive antenna. This is not applicable to base station antenna applications, since the two-way communication system consists of a base station and a cellular phone, instead of two equivalent antennas. Leeper [10] relied on difference sets to construct massively thinned phased arrays, from which more than half of the antenna elements were removed. The peak sidelobe level produced by these arrays is better than that produced by a randomly placed array, but a detailed performance comparison was not made. Similarly, Oliveri exploited almost difference sets in the synthesis of sparse linear [11] and planar [12] arrays. With knowledge of the array aperture, the thinning factor and the autocorrelation function, arrays can be synthesized. Numerical results show that these arrays exhibit a lower peak sidelobe level than random arrays.

Since each element in a thinned array is either off or on, it can be represented by a zero or a one. This binary nature lends itself well to optimization methods [16, 19], elaborated upon in Section 2.3. Thinning is mostly applied to very large antenna arrays where the grid dimensions are small relative to the aperture dimension, so the quantization error which is introduced by grid's restrictions does not matter much. Thinning has the disadvantage that the grid still implies strong restrictions in the form of regularity, which causes shadowing.

Placing elements completely randomly ensures that the antenna elements are distributed aperiodically, but the performance is not guaranteed; it depends on the random distribution on which the placement is based. In the 1960s, Unz [23] first proposed distributing the elements of a linear array arbitrarily to gain more degrees of freedom in the design. However, due to its random nature, little can be said of the performance of a

random antenna array. Maffett [24] formulated a method to describe the array factor of a stochastically placed antenna array in a statistic manner. In the 1970s, Steinberg [15, 25] set out to quantify the peak sidelobe level of a random array and found that it performed as well as an algorithmically thinned array, provided that it contained enough elements for the statistical approximations to be valid. Since then, many algorithms have been proposed, thereby outperforming random methods [10, 18, 26, 27]. Combinations of random and deterministic antenna distributions have been proposed by for example Kim [28], who used pseudo-random fractal structures, and Kerby [29], who used periodically placed random subarrays.

Placing elements along concentric rings is another way to cover a two-dimensional aperture while maintaining an easy to describe structure [18, 19, 30–39]. An indication of the resulting structure is given in Figure 2.1. Since the rings are circularly symmetrical, only the radius and the number of elements in each ring characterise the complete ring. Due to this property, the degrees of freedom are limited, which effectively reduces the two-dimensional problem to a one-dimensional problem. Density tapering and optimization approaches can thus be effectively applied to such a geometry. Since this layout possesses much symmetry, measures have to be taken to avoid shadowing. One approach is to apply a progressive angular shift to each ring to reduce this effect [18]. The inherent symmetry of such arrays ensures that the behaviour is similar for all ϕ. As will be seen later, the fact that this topology only provides a limited number of different radial coordinates, its accuracy and thus applicability for density tapering is limited.

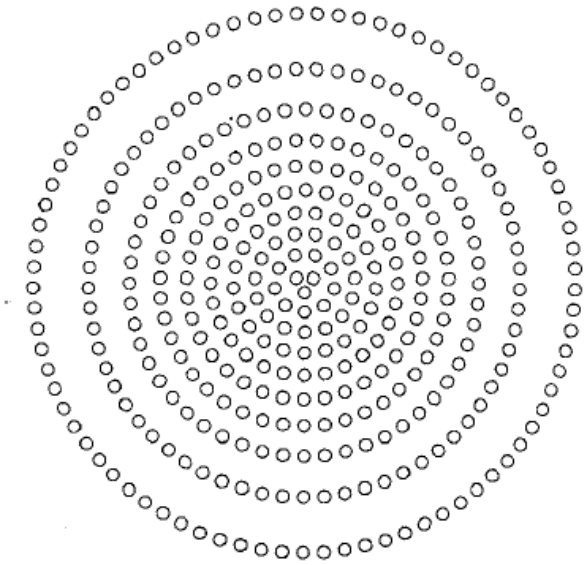

Figure 2.1: Topology of a concentric ring array [30].

Placing elements along a space-filling curve such as the Peano-Gosper curve can also have beneficial characteristics [26, 40–44]. In 2003, Werner [26] first investigated the radiation characteristics of an antenna array based on the family of space-filling and self-avoiding Peano-Gosper curves. Uniformly distributing elements along this curve results in a planar configuration on a hexagonal grid enclosed by a Koch curve. This property ensures that the array possesses the same grating lobe suppression as a hexagonal grid, whilst exhibiting a lower sidelobe level [41]. Despite this attractive property, the original Peano-Gosper array's antenna elements are still placed on a regular (hexagonal) grid, which causes shadowing in the same way as a regular array would. Researchers therefore set out to perturb the elements' locations along the curve to provide some irregularity. For instance, Bogard [42] applied a genetic algorithm optimization method to perturb the elements' locations. Spence [43] took the concept further to include the whole set of Gosper curves. These additional techniques overcome the disadvantage of regularity, and make the Peano-Gosper array approach feasible. An example of the Peano-Gosper array is given in Figure 2.2.

Placing elements using aperiodic tiles is another method based on a mathematical concept [27, 45–55]. The existence of sets of shapes capable of filling a plane aperiodically was proven in the early 1960s [46]. In 1974, Penrose [45] devised an aperiodic set consisting of only two tiles, a portion of which can be seen in Figure 2.3. This Penrose tiling is among the most often studied and best known aperiodic patterns. Such tiling provides aperiodicity while offering a fairly uniform distribution of elements in the aperture. Further-

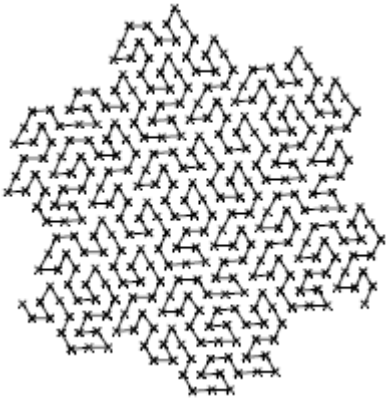

Figure 2.2: Topology of a Peano-Gosper array [42].

more, tiling sets are inherently modular, which may be advantageous in the manufacturing process. These properties make them viable for sparse antenna array formation. Pierro [27] identified these advantages and applied different tiling sets to devise array geometries, which exhibited desirable radiation characteristics. Besides the Penrose tiling, there are many other tiling sets, one of which is the Danzer tiling which possesses similar valuable characteristics to the Penrose tiling [47]. A portion of such tiling can be seen in Figure 2.4.

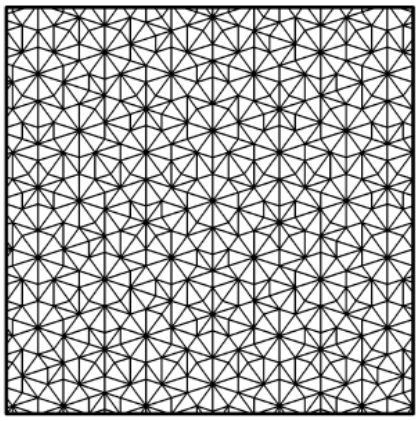

Figure 2.3: Portion of a Penrose tiling [47].

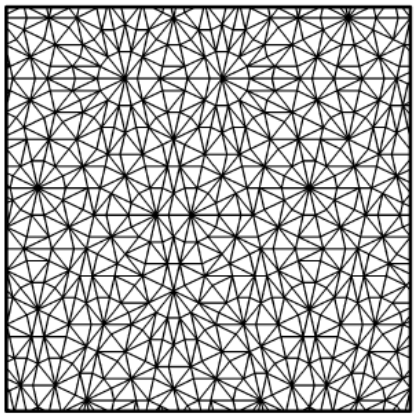

Figure 2.4: Portion of a Danzer tiling [47].

Placing elements along a curvilinear structure, such as the Fermat spiral, ensures low periodicity while remaining easy to describe mathematically [56–61]. Elements along such a spiral are placed according to these simple coordinate formulations [59]:

$$\rho_n = s\sqrt{\frac{n}{\pi}} \tag{2.1}$$

$$\phi_n = 2\pi n\beta_1 \tag{2.2}$$

where ρ_n is the distance from the spiral center to the n^{th} element, $n = 1, ..., N$ is the element's number, with N being the total number of elements in the array, s relates to the mean distance between neighbouring elements, ϕ_n is the angular displacement of the n^{th} element and the parameter β_1 controls the angular displacement between two consecutive elements, as can be seen in Figure 2.5. Although the spiral draws just one line, the choice of β_1 results in quite different spirals [58]. A special case occurs if the divergence angle $\beta_1 = \frac{\sqrt{5}+1}{2}$, also known as the golden angle, appears. When constructing the spiral with this angle, the resulting arrangement resembles the distribution of sunflower seeds. Besides being visually appealing, this pattern ensures that the distance between neighbouring elements remains constant for each radiator. Since β_1 is an irrational number, there will never be an element that has the same angular position as another one, thus

avoiding any rotational periodicity [60] and shadowing. Each radial coordinate ρ_n is uniquely defined which offers more freedom to finely tune individual positions than other topologies such as the concentric ring array. These properties, combined with the fact that the sunflower pattern ensures a uniform distribution of elements in the aperture, makes this structure an attractive option. Due to these advantages, this topology will be taken as the starting point in the rest of this work.

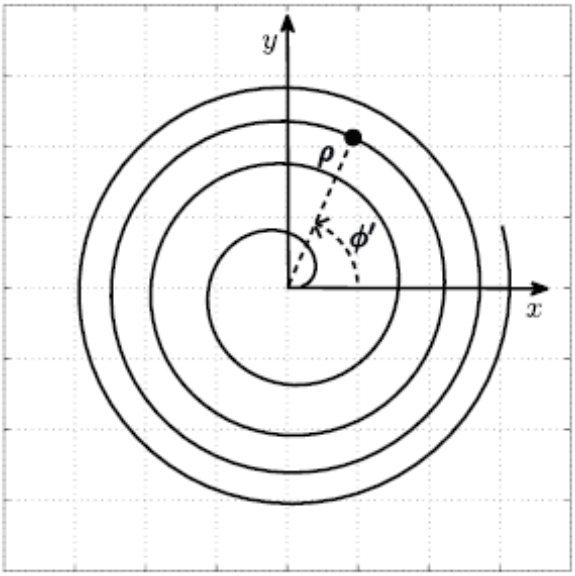

Figure 2.5: Fermat spiral [59].

While smartly placing the antenna elements may eliminate the appearance of grating lobes, their energy is distributed over the sidelobes, which remain relatively uncontrolled. There are roughly two ways to further enhance the radiation pattern: a deterministic method and a stochastic method. The deterministic method is based on an analytical tapering function, as will be elucidated in Section 2.2, and the stochastic method employs optimization algorithms to fulfil the task, on which Section 2.3 will elaborate.

2.2. DENSITY TAPERING

Similar to amplitude tapering, density tapering is used to approximate a certain continuous current distribution on an aperture, which is determined by the desired far-field radiation pattern. With amplitude tapering, the uniformly spaced elements' weights are adjusted to approximate the continuous current distribution. For closely spaced (about half a wavelength) elements, such an approximation is quite accurate [13]. Density tapering also approximates the desired current distribution, but in a different way: the locations of the elements are chosen in order to influence the element density and thus the current density, while keeping the amplitude weights constant. The main advantage is that each antenna element is uniformly excited, so that the amplifiers powering the antennas can be operated at the same, efficient, working point [62].

Willey [13] introduced density tapering as a way of reducing the number of antenna elements in an aperture while retaining good radiation pattern characteristics. For linear arrays, the spacing between elements is adjusted to produce an element density which complies with a tapering function such as a Taylor function. The two-dimensional case is also discussed, although only for a circular aperture. Here, the density taper is applied by thinning a uniformly filled aperture.

In [14], Skolnik designed density tapered antenna arrays by statistically thinning the aperture, using the tapering function as a probability density function. Such an approach is viable when the number of elements is very large so that the resulting density accurately represents the probability density function. In this work, the number of antenna elements is not sufficiently large to make this approximation valid. Furthermore, Skolnik states that in a planar array of 10,000 elements the sidelobes are determined more by the number of elements than by the type of tapering function. This last statement is confirmed by Harrington [63] and Andreasen [64], who varied the inter-element distance for symmetric linear arrays in an endeavour to minimize the sidelobe level for long linear arrays. Andreasen reported that the sidelobe level is predominantly

determined by the number of antenna elements, and that it decreases linearly with the number of elements.

Lo [65] critically reviewed density tapering methods from the 1960s as applied to linear arrays. It was found that due to the statistical nature of the approaches, most of the arrays that can be designed using these methods exhibit worse performance than reported. However, this is unsurprising since researchers tend to report the best cases in their publications. The disappointing results may also be attributed to the fact that the investigated antennas are quite small so the tapering function was only roughly approximated.

Anderson [66] identified the problems caused by the regularity which is still present with (statistically) thinned arrays and proposes a density taper method based on radial warping. This method eliminates the grid which is present with thinned arrays to prevent grating lobes at the cost of higher average sidelobes. The energy is mostly concentrated in the far-out sidelobes, which will be significantly attenuated by the individual elements' radiation patterns in Anderson's envisioned application.

A comparison with amplitude tapering is made by Kuo [67] and Toso [62]. Kuo applied the Taylor tapering function to a concentric hexagonal ring array consisting of 271 elements using density tapering and amplitude tapering and then compared the two approaches. A typical hexagonal array produced near-in sidelobes with about -17 dB power with respect to the main lobe. The amplitude tapered array and density tapered array both resulted in a near-in sidelobe level of -23 dB. The procedure was repeated for the arrays when scanned 9 degrees from boresight, where the amplitude tapered array outperforms the density tapered array by about 3 dB. Kuo concludes that density tapering can achieve similar results to amplitude tapering while providing the advantage that the amplifiers can be operated more efficiently since the antenna elements have uniform excitation. A similar comparison was made by Toso [62], although in this communication the two tapering strategies were only applied to linear arrays. A preliminary comparison was made and it was found that density tapering shows high potential in terms of a reduction in the number of elements, control points and amplifiers while improving the overall antenna power efficiency. These effects were clear from the comparison between linear arrays of several different sizes ranging from 10 to 20 elements. It is shown that there is a minimum number of elements from which the tapering distribution can be accurately approximated.

Suarez [68] applied several different tapering functions to a 16-element linear array with average inter element distance larger than a wavelength. The objective was to reduce the grating lobes which would be present in such an array without tapering. Instead of the usual grating lobes, 'pseudo-grating lobes' were formed, much further away from boresight and with more than -3 dB less power than the grating lobes. With non-isotropic radiators, the power level of such lobes is comparable to the power level of the sidelobes. This was confirmed by constructing such an array with simple patch antennas.

Both Vigano [59] and Ramalli [60] employed a Fermat spiral combined with density tapering to design a circular antenna array. Vigano placed antenna elements on a Fermat spiral where the angular positions were determined by Equation 2.2, and the radii were determined by a Taylor tapering function. Ramalli considered arrays with 256 elements and varying aperture size, tapering function and element size. It was found that density tapering performs more uniformly for different scanning angles than amplitude tapering.

Keizer [22] proposed two analytical methods based on Willey [13] for thinning a square or circular planar array according to a tapering function and reported that the beamwidth was comparable to the completely filled alternative, while the sidelobes were lower. The method is aimed specifically at arrays with a diameter of more than 100λ, so it is not interesting for me.

Density tapering offers a deterministic approach to enhance the radiation pattern and is shown to have high potential. Due to the fact that density tapering methods set out to approximate a continuous tapering function, the approximation gets better as the number of elements increases. It remains to be seen to what extent the continuous tapering function can accurately be approximated by a spatially undersampling sparse array.

Some array layouts are more suitable for density tapering, such as the concentric rings and spiral topology, since their element density can conveniently be altered by changing the radial coordinates of the elements and because of their rotational symmetry. Thinning approaches are less feasible for this method, since the fixed positions imposed by the grid lead to a large number of elements that are needed to accurately approximate the tapering function.

Since the initial reason for choosing a sparse array is the heat dissipation, the fact that density tapering allows the amplifiers to operate at the same efficient power point makes it a sensible strategy to be used. Chapter 3 discusses how analytical density tapering is applied in this work.

2.3. OPTIMIZATION

Optimization methods based on stochastic processes can also be employed to tune antenna element's coordinates and influence the radiation pattern of the antenna array. Several optimization algorithms are presented in the literature, the genetic algorithm of which is used most often. Therefore, Section 2.3.1 will cover such optimization approaches, and Section 2.3.2 will elaborate on the other algorithms.

2.3.1. GENETIC ALGORITHMS

Haupt [16] first recognized genetic algorithms [69] as an optimization method suitable for array thinning. The binary nature of the thinning concept lends itself well to such an algorithm, since genetic algorithms are binary by nature as well. Continuous parameters therefore need to be quantized [70, 71]. By applying a genetic algorithm to a thinned 200 element antenna array, Haupt achieved a relative sidelobe level of -20 dB.

Bray [72] used a genetic algorithm to optimize a linear array while scanning its beam. By starting out with a periodic array and by then introducing perturbations to the position of each element in the array, a maximum sidelobe level of about -10 dB was achieved when scanning from 0 to 60 degrees from broadside for an 8 element array with an initial spacing of 0.8 wavelength. For a 16 element array the results improved by 3 dB. Further improvements were expected when the maximum scan angle is decreased or when the number of elements is increased. Additionally, the input impedance of the elements was limited to a certain range to keep the elements matched well.

Bogard [42] achieved a 30 degree conical scanning beam with a minimum inter-element distance of 1.13 wavelength and an average inter-element distance of 1.69 wavelength by perturbing the positions in the first stage of the Peano-Gosper fractile array. In this region, no grating lobes appear and a maximum sidelobe level of -10.12 dB for a stage 4 (2402 elements), -9.05 dB for a stage 3 (344 elements) and -7.34 dB for a stage 2 (50 elements) array was achieved. In [44], Spence reported similar conclusions, and included a full wave simulation to investigate the mutual coupling effect, which was found to have only a minor influence on the radiation pattern. Spence [43] extended the above approach to a generalized class of Gosper curves. While this generalized class offered an expansion of possibilities in terms of the number of elements, the performance was found to be similar.

Chen [73] applied a genetic algorithm to optimize the antenna elements' positions within a certain boundary. A maximum sidelobe level of -18 dB was achieved for a 100 element array, spaced more than half a wavelength apart in an aperture of 9.5 by 4.5 wavelength.

Spence [53] elaborated on his earlier paper [47] by introducing a multi-objective optimization approach. Where [47] only optimized with respect to the side lobe level, [53] also optimized the degree of thinning in an attempt to simultaneously minimize the number of elements in the array. Essentially, this new approach only modified the cost function of the genetic algorithm. Spence achieved a -10.35 dB side lobe level with 398 elements with a minimum inter-element distance of 3.5 wavelength.

Rocca [52] applied a genetic algorithm to the polyomino-tiling approach proposed by Mailloux [49]. By subdividing the aperture into polyomino tiles a certain aperiodicity is introduced. Rocca then optimized the position and orientation of these subarrays. A maximum sidelobe level of -22.25 dB was reported for an array with 1567 elements and a minimum inter-element distance of 0.9 wavelength.

2.3.2. OTHER OPTIMIZATION METHODS

While genetic algorithms are widely used, other optimization methods exist that can be applied to the design of antenna arrays. This section will list some with their performances as reported in the literature.

Originally, elementary numerical iterative methods such as the steepest descent [74, 75] and the iterative least squares method [76] were used to optimize linear antenna arrays with respect to a desired radiation pattern. However, since the antenna array synthesis problem is not convex, such algorithms may get stuck in local minima, resulting in a suboptimal solution. Clavier [77] avoided this risk by first optimizing globally and then applying a gradient based optimizer as a last step to locally tune the antenna elements' locations.

Simulated annealing is another optimization method which is used to synthesize linear antenna arrays [78]. This technique, which is based on the behaviour of molecules in the cooling process of materials, was applied by Murino [78] to optimize the antenna elements' positions while sticking to a half wavelength grid. For a 50 wavelength long array consisting of 25 antenna elements, this resulted in a peak sidelobe level of about -12 dB. When the weights of the individual elements are also optimized, a peak sidelobe level of -13.5 dB was achieved.

Particle swarm optimization originates from the study of synchronous bird flocking and fish schooling

and was identified as an optimization method by Kennedy [79]. Contrary to classical methods that need calculations of the derivative, and similar to genetic algorithm optimization, particle swarm optimization is straightforward to implement as it only requires elementary mathematical operations. Boeringer [80] applied such an algorithm to a linear array to satisfy a predetermined radiation pattern. This was done alongside a genetic algorithm to explore the differences. It was found that both methods obtained satisfying results, and it was suggested that one algorithm might perform better in some situations whereas the other might perform better in other situations. It was concluded that the particle swarm algorithm itself is highly robust yet simple to implement, and it pursues different routes through the problem's set of possible configurations from other optimization methods.

Similar to genetic algorithms, differential evolution is based on the competitive mechanisms of natural selection, and was introduced by Storn [81]. Rocca [82] presented a survey of differential evolution applied to electromagnetics. It was applied to antenna array synthesis for the planar case solely as a hybrid method combined with a genetic algorithm [83]. First, a linear array was optimized using a differential evolution algorithm, after which a plane was filled with these arrays and thinning was performed by a genetic algorithm. The resulting array consists of 248 elements with an inter-element distance between half and 1.1 wavelength, and it exhibits a peak side lobe level of about -25 dB.

Another class of optimization methods was presented by Sahalos [84] termed the orthogonal methods. Sahalos outlined several procedures suitable for antenna array synthesis. However, solid performance results were not given and the orthogonal methods can get stuck in local optima [85]. Kaifas [86] proposed a relaxed constraint approach, which is an extension of the orthogonal method, to the optimization of a planar antenna array. In addition to satisfying a prescribed radiation pattern, the optimization produced a physically realizable layout, which is often not taken into account in other optimization approaches.

Bucci [39] exploited the rotational symmetry of concentric ring arrays to apply convex programming minimization techniques. Since the optimization was applied to arrays with concentric rings topology, the number of degrees of freedom was greatly reduced; only the number of elements in each ring and the radii of the rings were varied. Bucci focused on pencil beam arrays with a small scanning region, such as those used in satellite communication systems. A peak relative sidelobe level of about -20 dB is achieved.

In [55], Gregory synthesized planar antenna arrays according to an optimization method which employs the covariance matrix adaptation evolutionary strategy (CMA-ES) which was previously applied to other electromagnetic problems such as linear array optimization [87]. This evolution theory based optimization method performs well for problems with large dimensionality. The lack of translational symmetry in rotationally symmetric structures such as concentric rings, spiral or aperiodic tiling layouts is used as a framework of designing antenna arrays. The circular aperture was divided into wedges, such that only one wedge was optimized to reduce computational costs. The fact that the array factor is symmetric due to the rotational symmetry of the structure decreases the computational burden further. Most of the proposed arrays had several hundred antenna elements, but one example was shown for a 70 element array, which had a peak side lobe level of -8.4 dB with a minimum inter-element distance of 4λ. While such a large separation is unnecessary for my application, it shows that the method is also applicable to arrays with this number of elements.

Ha [88] approached the problem similarly to Chen [73], but used a Bayesian Optimization Algorithm to place the antenna elements in the quadrant. The BOA is a global optimization method also based on evolutionary mechanisms. Ha used a modified version which has a more elaborate mutation scheme. A 108 element array was presented and the peak sidelobe levels are -22 dB and -28.5 dB in the yz- and xz-plane, respectively. The results were compared to Chen's and a performance improvement was reported, although only the array factor in the main planes was presented.

Many of the above methods sacrifice a significant amount of degrees of freedom in order not to tackle the array layout problem directly.

To directly optimize each antenna element's x and y coordinate in an array is a problem with many variables to be optimized. In addition, calculations of the resulting radiation pattern are quite elaborate, making a straightforward optimization of all elements too computationally intensive. Therefore, researchers have sought for ways to reduce the amount of variables to be optimized and place restrictions on the search space. One way to do this is by choosing a base array layout with limited degrees of freedom, such as the concentric rings [39], which effectively reduces the two-dimensional problem to a one-dimensional one. One might also optimize a section of the array layout, which is then repeated to form the complete array [55]. Similarly, Bogard [42] optimized only the first stage of the Peano-Gosper curve, and repeated this pattern to fill the whole aperture. Also, Chen [73] optimized a quarter of the area of the aperture, and then filled the aperture by dupli-

cating this section symmetrically. Thinned arrays lend themselves well to discrete optimization approaches, since each antenna element can be replaced by a zero or a one [16].

On top of that, many publications only optimize the array factor to reduce computational costs. While such calculations are much quicker, they can be deceptive when the radiation pattern of the individual element and coupling effects are not taken into account.

Besides simplifying the problem by reducing the amount of variables, the choice of function which determines how good the solution is must also be made. Ideally, this cost function constitutes the performance of the array exactly, so the resulting radiation pattern as calculated by a full wave simulator should be taken. However, to speed up calculations, it is common to consider only the array factor. Furthermore, this cost function must result in a single value in order to be able to compare different realizations of the algorithm and choose the better one. Herein lies the challenge for optimization based antenna array synthesis: how to capture the quality of an array in one scalar value. In most cases, only one metric is used such as the peak sidelobe level, although other metrics, such as inter-element distance, are also important. By introducing weights to each metric a complete cost function may be formulated, but the difficulty then lies in what the weights should be.

This constitutes the fundamental flip side: although the freedom that optimization methods offer is valuable, challenges arise in the form of cost function and what to optimize. In Chapter 4, a genetic algorithm, combined with a density tapering technique, is employed in an effort to influence the array factor by certain requirements.

3

Density Tapering

A tapering function is a window that is designed to fulfill certain characteristics in the Fourier-transformed domain. Several analytical window functions exist, such as the Chebyshev or Taylor window functions. Appendix A gives an introduction to the well-known linear window functions and elaborates on the circular Taylor window, and its differences with the linear window. Since the window function is used as a current density distribution, these terms will be used interchangeably.

Throughout this work, the method of analysis used is explained in Appendix B. This appendix discusses the use of the k-domain and the techniques that can be exploited to allow for a quick analysis of a topology's performance.

This chapter will discuss the technique, procedure and results of applying an analytical density tapering function to the antenna array.

3.1. Continuous Current Distribution

Using Equation A.1, a circularly symmetric current distribution on an aperture can be designed that provides a certain sidelobe level for the first $\bar{n}$ sidelobes, and monotonically decreasing sidelobes beyond. In general, any combination of parameters $\bar{n}$ and SLL may be chosen, with a corresponding Taylor window. In this work, $\bar{n} = 10$ and $SLL = -25$ dB. The resulting current distribution $A(\tilde{r})$ as a function of the normalized radius $\tilde{r}$ is shown in Figure 3.1. The convenience of the high current density near the edges is explained Appendix A.

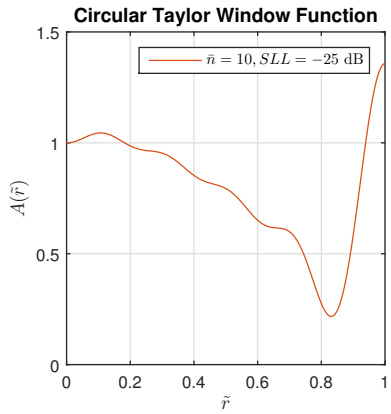

Figure 3.1: Circular Taylor Window Function with $\bar{n} = 10$ and $SLL = -25$ dB.

This window function is used as a circularly symmetric current distribution to fill a circular aperture. In Figure 3.2, this aperture is shown with its current distribution. The pattern of Figure 3.1 can be recognized: high current density in the center, gradually descending towards the minimum and a peak near the edge of the aperture. Using the analysis method presented in Appendix B, the resulting radiation pattern can be found. This radiation pattern in k-domain is shown in Figure 3.3. A cut of the pattern for $\phi = 0°$ is displayed in Figure 3.4.

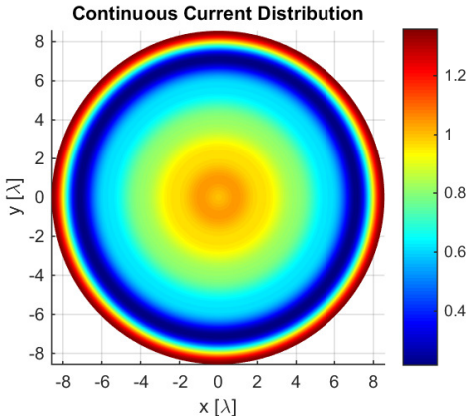

Figure 3.2: Continuous current distribution according to the Taylor window with $\bar{n} = 10, SLL = -25$ dB.

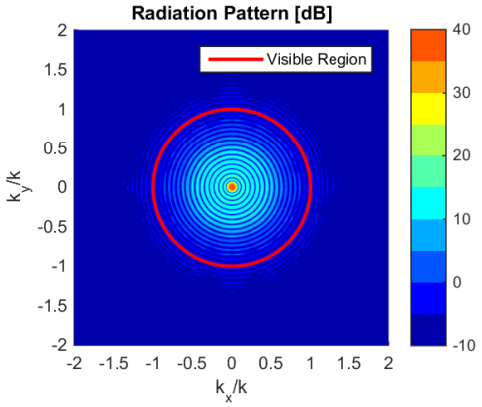

Figure 3.3: Radiation pattern of the continuous current distribution.

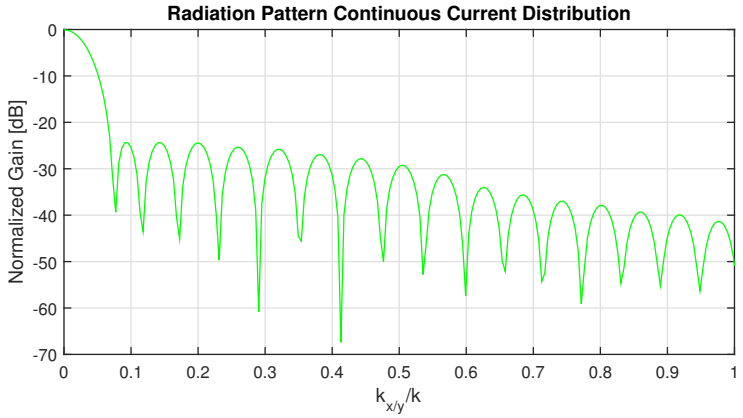

Figure 3.4: Radiation pattern of the continuous aperture for $\phi = 0°$.

In Figure 3.4, it can be seen that the sidelobes satisfy the Taylor window's specifications, as they remain below the specified -25 dB level, although although not all of the first 10 sidelobes exactly come to this value. This may be due to inherent discretizations in the numerical calculations.

It is noted that this continuous situation is the ideal situation. Populating the aperture with discrete elements to make up the antenna array is a mere discretization and thus approximation of this distribution. Therefore, the above results and figures will be used as a benchmark against which the forthcoming array topologies will be tested.

3.2. CURRENT DENSITY DISCRETIZATION

This section will explain the process of approximating the desired continuous current distribution by populating the aperture with N discrete antenna elements. To this end, the elements' radial coordinates are modified to approximate the desired current density. Since the desired current distribution is circularly symmetric, only the radial coordinate is changed. One of the reasons why the sunflower topology was chosen, is that each radiator has a unique angular coordinate (Equation 2.2) to prevent shadowing. Therefore, the angular coordinates will not be altered in this process. Although somewhat edited, the overall procedure outlined

by Vigano [59] is followed.

The radial coordinates ρ_n are determined by the following iterative algorithm.

First, the circular aperture is divided up into N rings, each centered around the origin and enclosing one element. This is illustrated in Figure 3.5. Here, the rings are shown for the center of the aperture. Every fifth ring is a continuous line to aid visibility. Adjusting the radii of these rings directly affects the current density: since each ring encloses exactly one element, the relative current density is inversely proportional to the enclosed area.

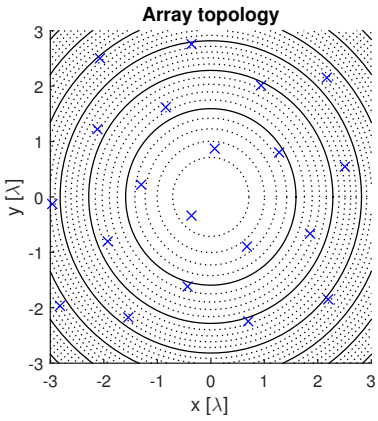

Figure 3.5: Center of tapered topology with element-enclosing rings visible.

The radii of these rings $R_n, n = 1,2\ldots N$, are calculated by applying [59]

$$2\pi \int_{R_{n-1}}^{R_n} A(r) r dr = \frac{2\pi}{N} \int_0^{R_{ap}} A(r) r dr \tag{3.1}$$

where ring n's inner radius is R_{n-1} and outer radius is R_n, $R_0 = 0$ and $R_N = R_{ap}$, where R_{ap} is the radius of the total aperture and $A(r)$ is the window function that serves as the current density function. While this window function can be any function, in this case $A(r)$ is given by the circular Taylor window function of Equation A.1. In this relation, the right side constitutes the total integral of the current distribution divided by N, which can be seen as the weighted current distribution per element. This equation ensures that R_n are chosen such that each ring encloses the same weighted current, which is the current of a single element.

With the radii of the rings, the radial coordinates of the elements can be calculated by applying [59]

$$2\pi \int_{R_{n-1}}^{\rho_n} A(r) r dr = \frac{2\pi}{2N} \int_0^{R_{ap}} A(r) r dr \tag{3.2}$$

which can be seen as choosing ρ_n as the weighted mean of the ring with outer radius R_n and inner radius R_{n-1}. Since the angular coordinates of the elements were already specified, with these equations the topology is fully described.

3.2.1. SPARSE ARRAY

In Figure 3.6, a 100 element array, synthesized using the above procedure with $\bar{n} = 10$, $SLL = -25$ dB, is shown.

The tapered topology is scaled to satisfy the 1.1λ minimum distance between elements condition, which causes the tapered array to cover a larger aperture than the untapered array due to the irregular spacing. The high element density near the edge of the aperture can be recognized in the figure. The middle of the topology is also relatively dense, and the region between is relatively sparse. This corresponds to the current density of the window function of Figure 3.1.

To verify the constructed current density as a function of the radius, the following procedure is executed. P rings are defined that each enclose N/P elements. The radii of these rings are defined as $R_p = R_{pN/P}, p = 1,2,\ldots P$. The area of ring p is $\pi(R_p^2 - R_{p-1}^2)$. Since each ring encloses the same number of elements N/P, the element density and thus current density in ring p is

$$\tilde{A}(p) = \frac{N/P}{\pi(R_p^2 - R_{p-1}^2)} \tag{3.3}$$

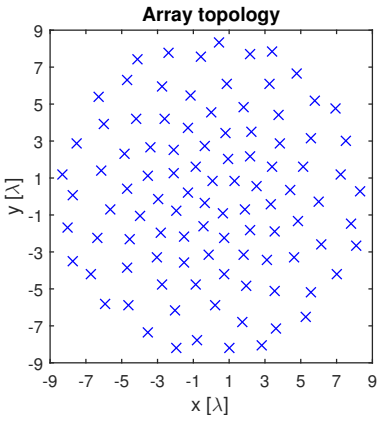

Figure 3.6: Topology of the tapered sunflower array.

A verification of the normalized current density in the density tapered array compared to the continuous window function for $P = N = 100$ is shown in Figure 3.7.

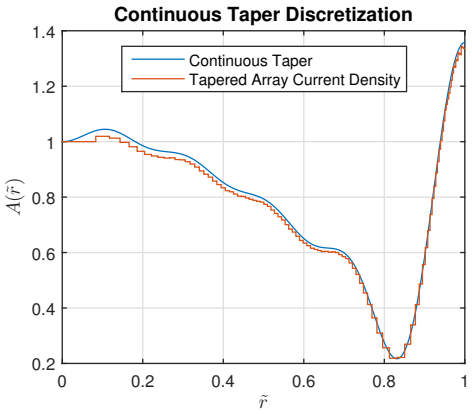

Figure 3.7: Discretization of tapering function.

From this figure, it seems that the approximation is quite accurate. The discretized curve follows the continuous curve quite precisely. Next, the array factor of the tapered array is calculated. The results are shown in Figures 3.9 and 3.10.

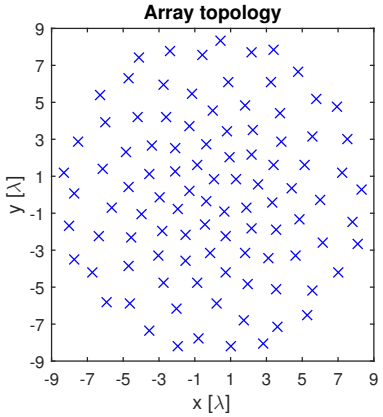

Figure 3.8: Topology of the sparse tapered sunflower array.

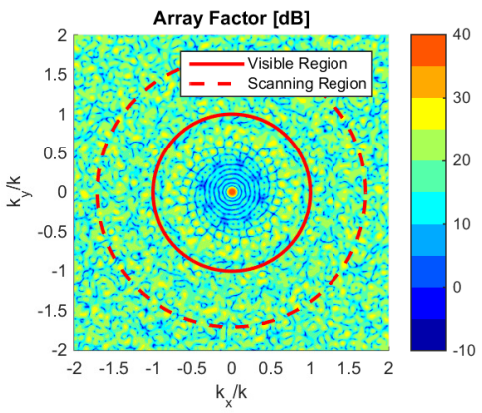

Figure 3.9: Array factor of the sparse tapered sunflower.

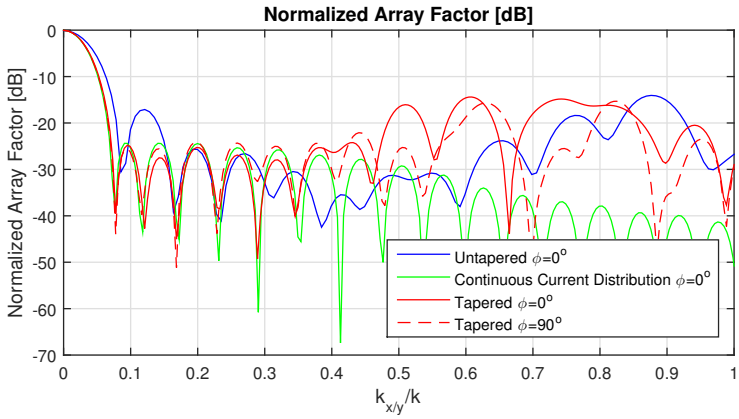

Figure 3.10: Array factor of the sparse tapered array for $\phi = 0°$ and $\phi = 90°$.

While the discretization appears quite accurate in Figure 3.7, the resulting array factor is only in agreement with the radiation pattern of the continuous aperture in a limited field of view. This is due to the fact that the current density is projected onto only one axis: r, so any information contained in the angular coordinates is lost. Since the array has a minimum distance between elements of 1.1λ, the array's sparsity can be seen as a spatial undersampling of the incoming wave. Therefore, the accuracy of the discretization is imperfect, which expresses itself in the fact that the array factor of the continuous distribution is approached in a limited field of view.

In Figure 3.10, a cut of the array factor can be seen. Up to a certain $k_{x/y}/k$, the tapered array follows the continuous radiation pattern accurately. The high first sidelobe, which is present in the untapered array, is suppressed. However, this comes at the cost of higher sidelobes in the region further away from the main beam.

The tapered sparse array accurately follows the specified continuous current distribution up to a certain $k_{x/y}/k$. Using Fourier knowledge and the tools that were explained in Appendix B, we can expect a more dense array to approximate the continuous current distribution's radiation pattern better. Compressing the array topology leads to an expansion of the array factor. A denser array will expand the array such that the accurately approximated region covers a larger region.

3.2.2. DENSE ARRAY

Instead of scaling the topology to achieve a minimum distance between elements of 1.1λ, the topology is now scaled to achieve a minimum distance between elements of 0.5λ, the distance needed by regular arrays to scan grating-lobe free, and the spacing that can be seen as the Nyquist criterion in space. Figure 3.11 displays the topology on the same axes as Figure 3.6 to illustrate the different sizes. The array factor in k-domain can be seen in Figure 3.12 and Figure 3.13 shows the array factor for $\phi = 0°$ and $\phi = 90°$.

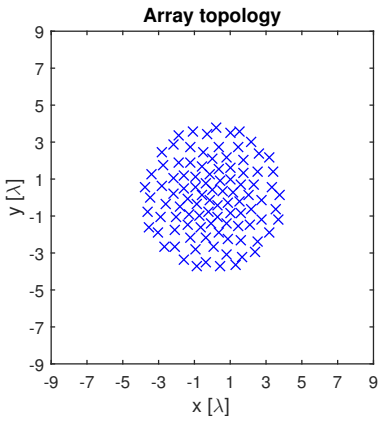

Figure 3.11: Topology of the dense tapered sunflower array.

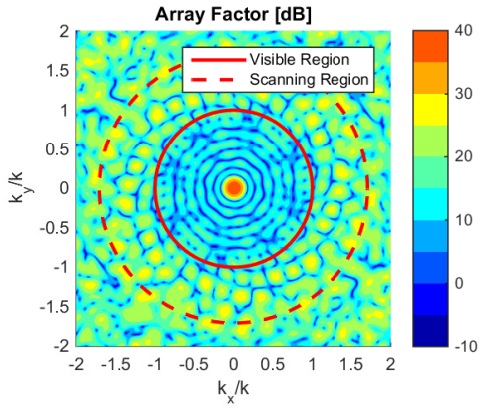

Figure 3.12: Array factor of the dense tapered sunflower.

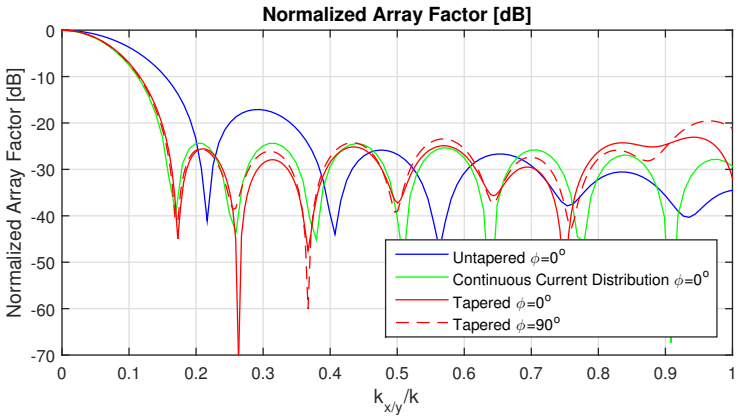

Figure 3.13: Array factor of the dense tapered array for $\phi = 0^\circ$ and $\phi = 90^\circ$.

As expected, the array factor pattern is stretched such that the sidelobes do not exceed -25 dB, apart from the edge of the visible region. The dense array barely undersamples the continuous current distribution. However, the denseness gives rise to increased coupling effects, which may deteriorate the actual accuracy of the approximation.

3.3. CONCLUSIONS

This chapter explained the procedure and results of density tapering using an analytical tapering function. A Taylor tapering window was applied as current density to a spiral array with 1.1λ minimum spacing between elements. The discretized sparse array's resulting array factor only approximated the continuous distribution's radiation pattern in a limited field of view. Thus, for the foreseen base station antenna array having 1.1λ spacing, density tapering is effective in a limited region.

The tapered array was then scaled down to make it dense in order to expand the field of view where the array's approximation is accurate. Approaching the Nyquist sampling criterion in space, this array approximated the continuous distribution's radiation pattern in almost the entire visible region. The dense array may suffer from more severe coupling effects. To investigate these effects, Chapter 5 will cover full electromagnetic wave simulations of both the sparse and the dense array topologies. Preceding Chapter 5, Chapter 4 introduces an optimization technique to stochastically develop the best current density distribution.

4

OPTIMIZATION

In addition to the analytical approach to density tapering described in Chapter 3, a genetic algorithm optimization approach is undertaken and explained in this chapter. There only exist a finite number of analytical window functions. The flexibility of optimization techniques gives the designer more freedom to express any requirements, as long as they are physically feasible. This freedom is its strength but also introduces an inherent challenge: to effectively employ an optimization algorithm, thought needs to go into the parameters and conditions of the algorithm.

A general explanation of genetic algorithms is given in Appendix C. This chapter will elaborate on how the algorithm is employed in this work. The possibilities of optimization techniques are endless. This work focused on several objectives to investigate to what extent optimization may be suitable as a means of antenna array design. Section 4.1 will explain the goals of the method and the way to quantify the array's performance. Section 4.2 elaborates on the parameters which are to be optimized and Section 4.3 explains the algorithm's parameters that are employed in this work.

Globally, the objectives are formulated as follows:

Firstly, a continuous current distribution is optimized with respect to a certain sidelobe level. The aperture is then populated with a varying number of elements to see how these array topologies' performance compares to the continuous aperture's. This approach is described in Section 4.4 and is comparable with the discretization of the density taper of Chapter 3.

Secondly, Section 4.5 describes how the discretized arrays are optimized to see whether an optimum is obtained that outperforms the array that uses the previously obtained continuous optimal distribution. This is an important question in the sense that if this is not the case, only one optimization has to be executed regardless of the number of elements in the array.

4.1. COST FUNCTION

As discussed in Section 2.3, it is very much up to the designer to provide the cost function of the genetic algorithm, and this is where the difficulty lies: the 'quality' of the realization should be captured in a single scalar value to be able to sort the different realizations. Optimizing the peak sidelobe level is simple, but can be deceiving since the antenna element's radiation pattern is not taken into account and does not contain any information on the rest of the sidelobes.

In this work, a mask on the array factor is used as cost function. This mask is free to choose, and may consist of several separate segments with different sidelobe levels. Any sidelobe in the mask's region that has a value higher than the mask's value is marked as a violation of the mask. The ratio of violated points to the total points in the mask's region is calculated and constitutes the cost function. Violations near the beginning of the mask are penalized heavily to restrict the beamwidth and to ensure that the whole aperture is utilized. The mask can be chosen freely to fulfill the requirements of any specific application. In this work, the mask will initially be set at -30 dB for $\sqrt{k_x^2 + k_y^2} > 0.1k$, corresponding to an elevation angle of about $6°$, to restrict the beamwidth.

4.2. PARAMETERS TO BE OPTIMIZED

The effectiveness of the optimization algorithm depends very much on the choice of what parameters are to be optimized. Optimizing each x and y coordinate directly would result in too many parameters and makes the search space too large. On the other hand, restricting the degrees of freedom too much and the solution is no longer optimal. In this work, the current density distribution is described as a polynomial with a finite number of coefficients, which are to be optimized. This limits the number of variables to be optimized to reduce the computational burden. The optimal current distribution, $A(r)$, is then used to obtain the radial coordinates of the elements by following the procedure described in Section 3.2. Again, the angular coordinates of the regular sunflower topology are kept to ensure the absence of shadowing.

The optimization algorithm describes the current distribution $A(r)$ as a fifth order polynomial, defined by six coefficients $p_n, n = 0, 1, \ldots, 5$:

$$A(r) = p_5 r^5 + p_4 r^4 + p_3 r^4 + p_2 r^2 + p_1 r + p_0 \tag{4.1}$$

Naturally, any order polynomial can be chosen, introducing a tradeoff between computational cost and degrees of freedom, which is linked to the optimality of the solution. The coefficients are quantized according to Equation C.2. The resolution of q_n, and thus p_n, is the smallest quantization level, given by

$$\text{resolution} = 2^{1-N_{pbit}} Q \tag{4.2}$$

This means that the range of q_n is given by

$$0 \leq q_n \leq 2Q - 2^{1-N_{pbit}} Q \tag{4.3}$$

To also allow for negative coefficients, the relation between q_n and p_n is chosen to be

$$p_n = q_n - Q \tag{4.4}$$

such that the range of p_n is given by

$$-Q \leq p_n \leq Q - 2^{1-N_{pbit}} Q \tag{4.5}$$

If $A(r) < 0$ for $0 \leq r \leq R_{ap}$, p_0 is adjusted such that $A(r) \geq 0$ for all $0 \leq r \leq R_{ap}$. Finally, $A(r)$ is normalized.

4.3. GENETIC ALGORITHM PARAMETERS

As explained in Appendix C, there are a number of parameters that need to be set for the genetic algorithm. Table 4.1 lists these, along with their influence on the behaviour of the algorithm [70] and the values that were mostly used in this work.

4.4. OPTIMIZING CONTINUOUS APERTURE

The first experiment consists of optimizing a continuous circularly symmetric current distribution on a circular aperture. The size of the aperture is the same as the sparse Taylor tapered array: $R_{ap} = 8.6\lambda$. As mentioned above, the mask on the radiation pattern is −30 dB for $\sqrt{k_x^2 + k_y^2} > 0.1k$.

In Figure 4.1, the optimized current distribution is shown, which is the result of the execution of the genetic algorithm with the parameters as specified in Table 4.1. A cut of the corresponding (circularly symmetric) radiation pattern is shown in Figure 4.2. The mask is denoted by the black dashed line.

The next step is to populate a discrete array using this current distribution. This is done by using the same procedure as described in Section 3.2. However, while Section 3.2 regulates the sparsity by scaling the entire array, in this section the aperture will contain a varying number of elements to vary the sparseness. Figures 4.3 and 4.4 show the resulting topologies for $N = 400$ and $N = 100$ elements, respectively.

The minimum inter-element spacing varies from 0.5λ to 1λ for the 400 element array, and from 1λ to 2λ for the 100 element array. The low density in the center of the aperture can be recognized, and the edges of the arrays are relatively unoccupied. In Figure 4.5, the array factor is shown for these arrays, tapered according to the optimized continuous current distribution for $N = 50, 100, 200$, and 400.

Similar to previous observations, the tapered arrays' array factors follow the continuous aperture's radiation pattern in a limited field of view. The extent to which the continuous distribution's characteristics are approximated depends on the sparseness: the more sparse the array is, the more narrow this field of view is.

Table 4.1: Parameters used in the genetic algorithm.

Parameter	Description	Influence on algorithm	In this work
N_{pbit}	Number of bits per parameter	More bits give greater accuracy but slower convergence	8
Q	Largest quantization level of q_n.	Larger Q expands the solution space but degrades the resolution.	2.5
M	Number of chromosomes in the population	Higher M gives better coverage of solution space but slower convergence.	40
-	Generating the initial population	Any prior knowledge may aid convergence.	Bernoulli distribution
$M2$	The number of chromosomes to keep	It can also be chosen to discard the chromosomes with a certain cost based on prior knowledge to speed up convergence.	$M/2$
mc	Mutation chance	Too low mc will result in the algorithm getting stuck in local optima, too high will impede convergence.	$4-8\%$ and the best chromosome is immune to mutation
-	End condition	Either a prespecified number of iterations, or a certain convergence condition may be used	Stop when converged or after 500 iterations

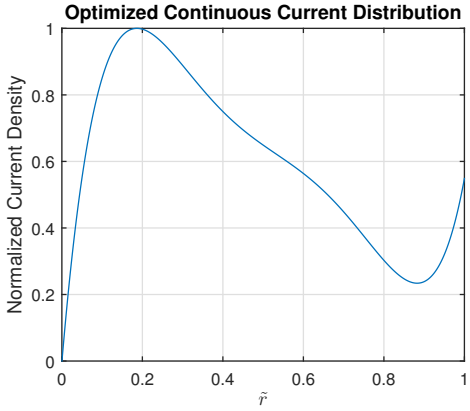

Figure 4.1: Optimal continuous current distribution.

4.5. OPTIMIZING DISCRETE ARRAY

Next, the question is whether the current distribution of the continuous current distribution is optimum also for the discretized finite element arrays. This is a valuable question because if this is the case, only one optimization needs to be executed for a certain set of requirements, regardless of the number of elements. In order to investigate this, a new mask is introduced for each array, which is slightly more demanding than the realized array factor with the continuous optimum. If the new discrete optimum cannot outperform the continuous optimal distribution, the latter is in fact optimum for the discrete situation as well.

400 ELEMENT ARRAY

First, the most dense array is taken. For this array, the previously used optimization mask is feasible in the visible region and thus stays the same. The discretely optimized distribution is shown in Figure 4.6.

It is evident that the results of the continuous current optimization are very closely related. The discrete optimum follows the continuous optimum narrowly, deviating only in the form of a more pronounced peak near the edge of the aperture. The resulting array and array factor are depicted in Figure 4.7 and 4.8, respectively.

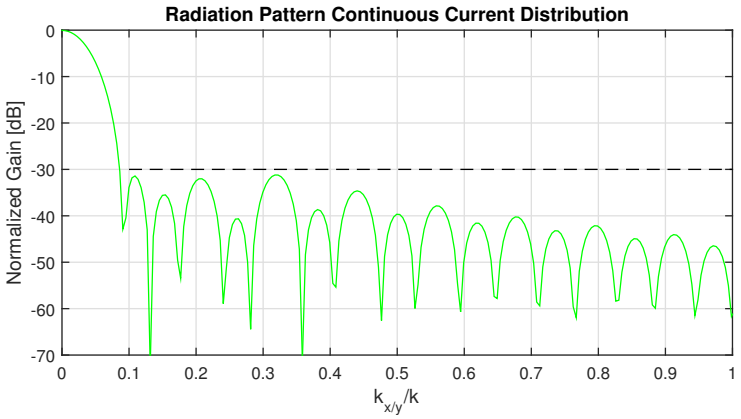

Figure 4.2: Radiation pattern of the optimal continuous current distribution.

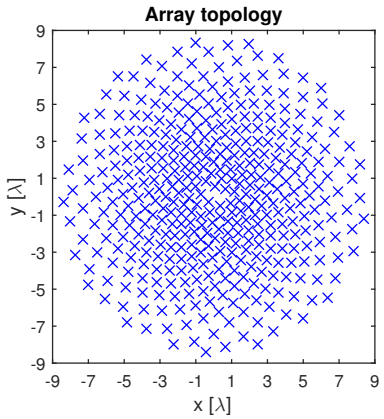

Figure 4.3: Topology of the 400 element array tapered with the optimal continuous current distribution.

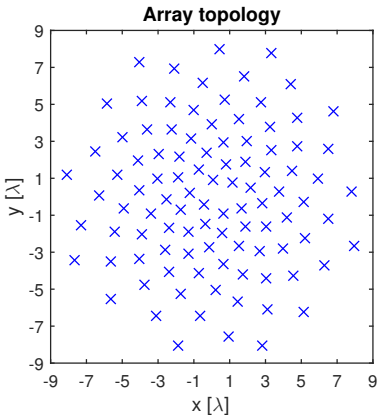

Figure 4.4: Topology of the 100 element array tapered with the optimal continuous current distribution.

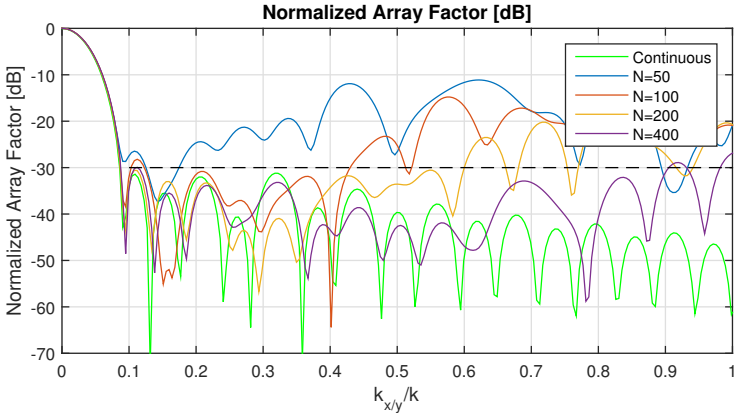

Figure 4.5: Array factor of the arrays with different number of elements based on the optimal continuous current distribution.

The blue curve depicts the array factor of the 400 element array that uses the continuous optimized current distribution while the red curve depicts the array factor of the discretely optimized array. Here it can be seen that the optimization mask is satisfied. The 400 element array's results when using the continuous optimized distribution were already satisfactory, and directly optimizing the discrete array does not result in a deviation in current density distribution. This suggests that for relatively dense arrays, optimizing a continuous distribution is sufficient. To see whether this is also valid as the array becomes more sparse, the following

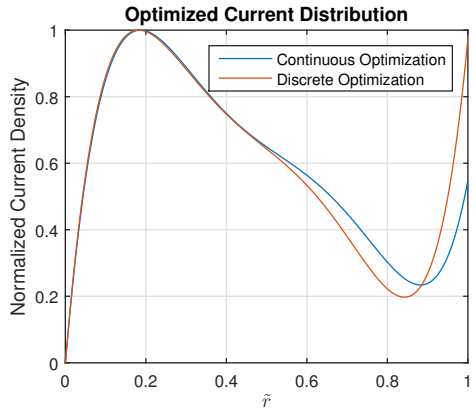

Figure 4.6: Optimal current distribution for the $N = 400$ element array.

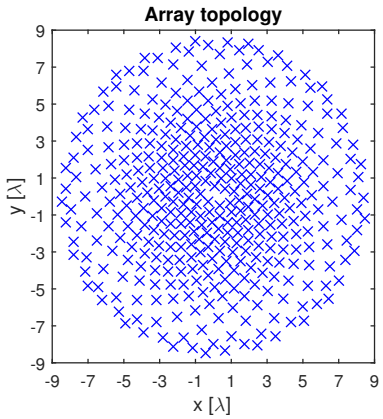

Figure 4.7: Topology of the 400 element array based on its dedicated optimal current distribution.

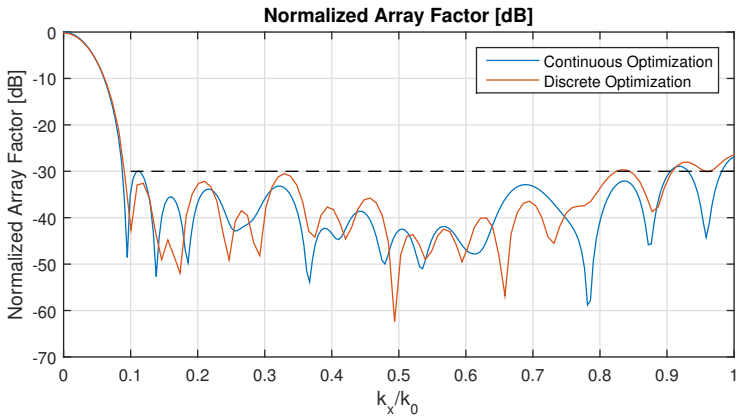

Figure 4.8: Array factor of the optimized 400 element array for $\phi = 0°$.

sections repeat the process for arrays with less elements.

200 ELEMENT ARRAY

The optimization mask for the 200 element array is slightly relaxed, to allow for realistic results. However, the outcomes and comparison to the continuous distribution is still valid because the optimal continuous distribution would be the same with this mask. The optimized distribution is shown in Figure 4.9, alongside the corresponding topology which is shown in Figure 4.10, and the resulting array factor is shown in Figure 4.11.

Similar to the 400 element array, the optimal current distribution deviates only marginally from the continuous optimum. Figure 4.11 shows that the array factors are comparable as well. The dedicated discrete optimization has led to a marginally wider main lobe, and the relatively high sidelobes also come into play slightly further away from the main beam.

100 ELEMENT ARRAY

Next, an array with 100 elements is optimized with respect to a suitable mask. The resulting optimal current distribution is shown in Figure 4.12, accompanied by the corresponding topology in Figure 4.13 and its array factor is shown in Figure 4.14.

Again, both optimal distributions bear much similarity. Even for such a sparse array, the optimal current distribution matches the continuous optimum. Figure 4.14 emphasizes this similarity, as the two array factors are very much alike. Thus, there is barely any performance difference between the discretely optimized current distribution and the continuous optimized current.

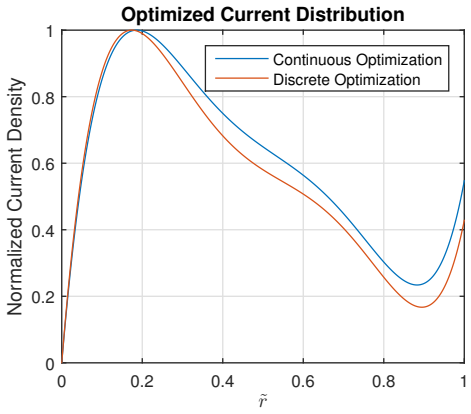

Figure 4.9: Optimal current distribution for the $N = 200$ element array.

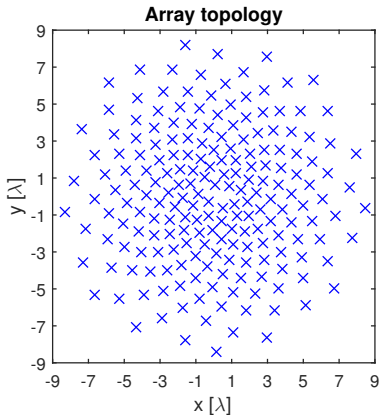

Figure 4.10: Topology of the 200 element array based on its dedicated optimal current distribution.

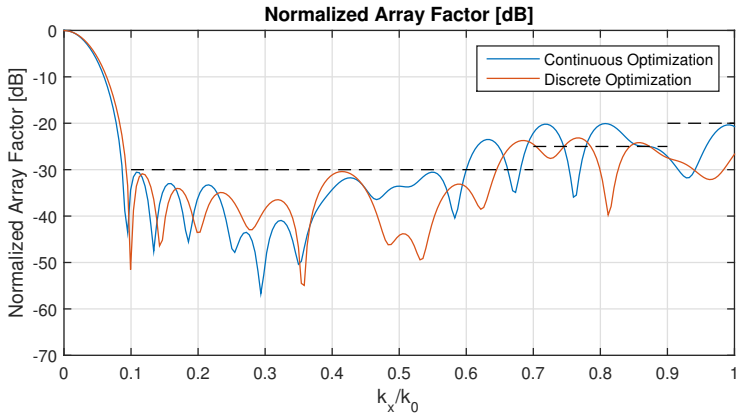

Figure 4.11: Array factor of the optimized 200 element array for $\phi = 0°$.

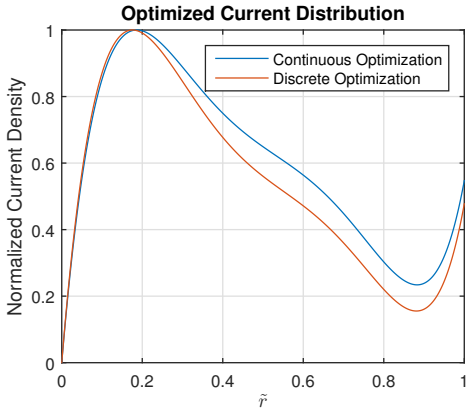

Figure 4.12: Optimal current distribution for the $N = 100$ element array.

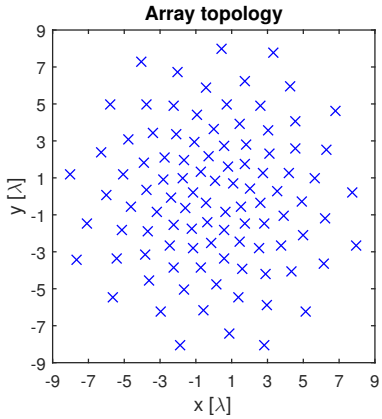

Figure 4.13: Topology of the 100 element array based on its dedicated optimal current distribution.

50 ELEMENT ARRAY

The same procedure was repeated for a 50 element array. The optimal distribution and corresponding topology can be seen in Figures 4.15 and 4.16.

It can be seen that even for such a sparse array, the optimum current distribution bears much similarity with the optimal continuous distribution. Apart from the region near the edge of the aperture, the similarity is striking.

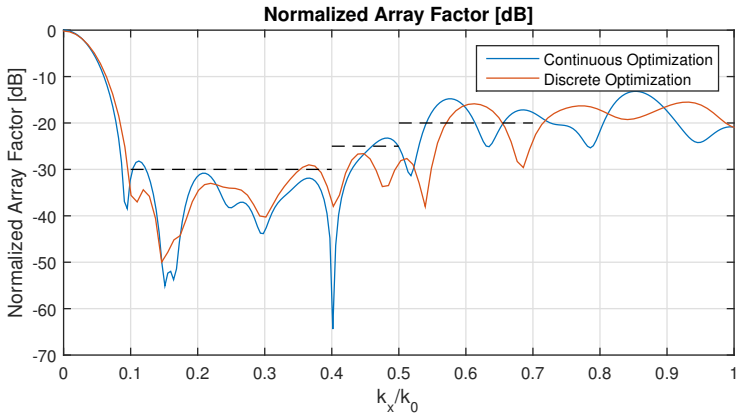

Figure 4.14: Array factor of the optimized 100 element array for $\phi = 0°$.

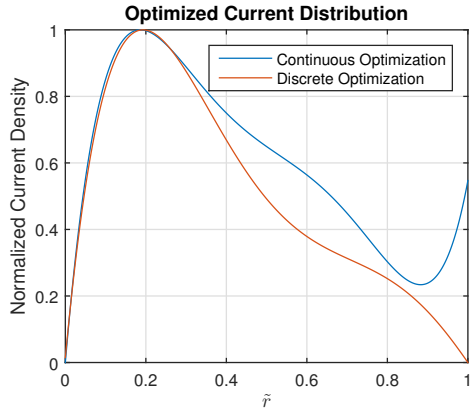

Figure 4.15: Optimal current distribution for the $N = 50$ element array.

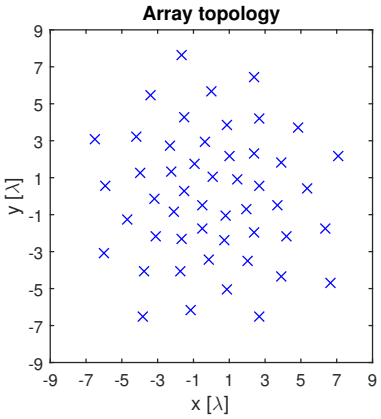

Figure 4.16: Topology of the 50 element array based on its dedicated optimal current distribution.

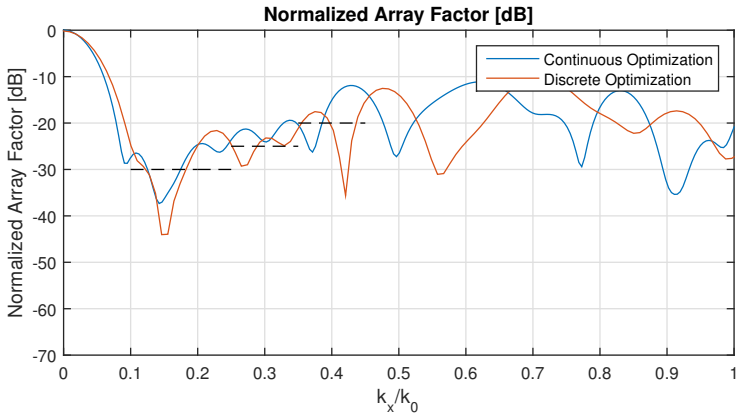

Figure 4.17: Array factor of the optimized 50 element array for $\phi = 0°$.

The resulting array factor, which can be found in Figure 4.17, shows little difference from the array factor computed with the continuous optimum distribution. While this sparse topology is gravely undersampling space, the optimal solution is still comparable to the continuous situation.

To summarize, the current density distribution was optimized for discrete arrays with varying sparsity and compared to the arrays obtained by using the optimal continuous distribution. The sparseness of the different finite arrays is illustrated in Figure 4.18, where a box plot of the distance to the nearest neighbour is

shown. The discrete optimized current distributions show remarkable similarity to the continuous optimum, as illustrated in Figure 4.19. For large N, the distributions barely differ, which was to be expected since this comes closest to a continuous current distribution. For decreasing N, the distributions deviate slightly, but the general pattern is similar. Even for a very sparse array, the general trend of the distribution is similar to the continuous optimum. This optimal distribution diverges only near the edge of the aperture.

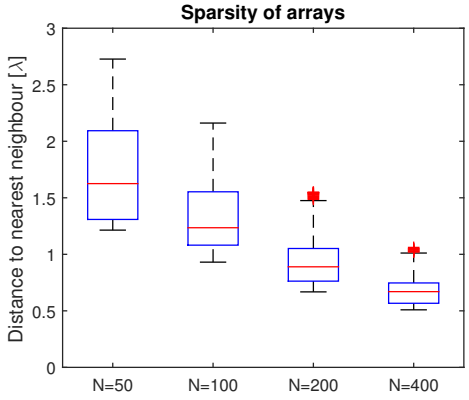

Figure 4.18: Box plot displaying each array's sparsity.

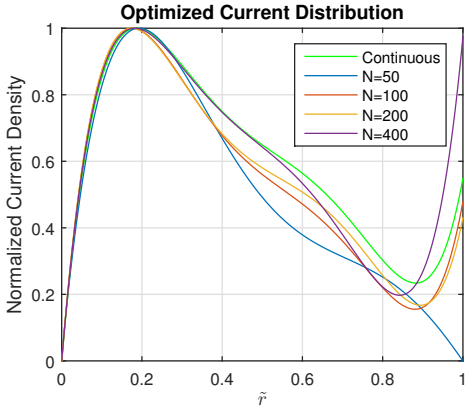

Figure 4.19: Optimal current distributions for continuous and discrete arrays.

The question can be posed whether this discrete array current distribution optimization is even comparable to the continuous optimization due to the different masks. However, if the discrete optimization's masks were to be used in the continuous situation, it would result in the same optimum. This is due to the fact that for the continuous case, only the section nearest to the main beam matters. The other sections are satisfied regardless of their height.

4.6. CONCLUSIONS

This chapter described how a genetic algorithm has been employed to optimize the current density distribution. The flexibility of the algorithm makes it a viable alternative to the analytical method presented in Chapter 3.

Populating an optimized continuous current distribution with a finite number of elements resulted in the array factor approximating the continuous distribution's radiation pattern in a limited field of view, depending on the sparseness of the array. This is in coherence with the observations of Chapter 3.

More significantly, this chapter provided the answer to the question whether the optimal current distribution of the continuous current distribution is also optimum for discretized finite element arrays. It was found that this is the case, such that when optimizing a planar antenna array, a single optimization of a continuous current density is sufficient, and practically optimal finite element arrays can be generated by using this current density distribution. For dense arrays, the optimum current distribution is the same as for a continuous aperture, and sparse arrays based on the optimum continuous current distribution show little performance degradation compared to a dedicated optimization of the finite element array. This is a valuable finding since only one optimization needs to be executed for a certain set of requirements to obtain the optimum current distribution for arrays containing any number of elements.

Pragmatically speaking, this chapter has not directly led to an improved array topology for the base station antenna array. However, the acquired insights may prove useful when the definite requirements for the antenna array are known. Also, if for some reason an improved cooling method is adapted that allows for a more dense array, the same current distribution can be used as for the sparse array since it was found that this distribution is optimal for both cases.

5

Full Electromagnetic Wave Simulation Results and Analysis

To investigate the performance of the tapered arrays in a more realistic environment, the analytically tapered arrays of Chapter 3 are analyzed using FEKO full electromagnetic wave simulation software. Both sparse and dense arrays will be examined and compared to their untapered counterparts. The full wave simulation takes into account coupling effects and will provide more realistic results than looking only at the array factor. Mutual coupling effects are unpredictable and undesirable, and their presence can seriously limit the array's performance. The influence of coupling can be considered from both ends of the antenna array: from the circuitry side and from the radiating side. The first involves the influence on the reflection coefficient, a quantity critical to the design of the circuitry behind the antenna. The latter is the fact that coupling may exhibit itself in deteriorating the radiation pattern. Both quantities will be examined in this chapter.

5.1. Patch Antenna

For a theoretical analysis of the patch (microstrip) antenna, the reader is referred to [2] or other standard literature. The emphasis of this work does not lie on the choice of radiator, and a simple rectangular patch antenna is chosen with the following parameters:

$$W = 0.30\ \lambda$$

$$L = 0.23\ \lambda$$

$$h = 508\ \mu\text{m}$$

$$\varepsilon_r = 2.2$$

The dimensions of the patch are quite small to provide a large beamwidth, in order to have -3 dB scan loss at the maximum scanning angle $\theta_{max} = 45°$, which is required for the envisioned base station antenna array application.

5.2. Sparse Array

First, the radiation patterns of the untapered and tapered sparse array will be compared. For boresight operation, the $\phi = 0°$ cut of the radiation pattern is shown in Figure 5.1.

It can be seen that the first sidelobe is suppressed by the tapering, but further from the main beam there exists a region with relatively high sidelobes. Beyond 60°, the sidelobes are again lower for the tapered array. The gain of the tapered array is slightly higher: 26.8 dB compared to 26.1 dB for the untapered sunflower. This suggests that coupling effects are more severe for the untapered array. Also, the peak sidelobe level is somewhat better for the tapered array: 16.3 dB versus 16.1 dB. The position of the peak sidelobe is the main difference.

For the maximum scan angle, $\theta_0 = 45°$, the results are shown in Figure 5.2.

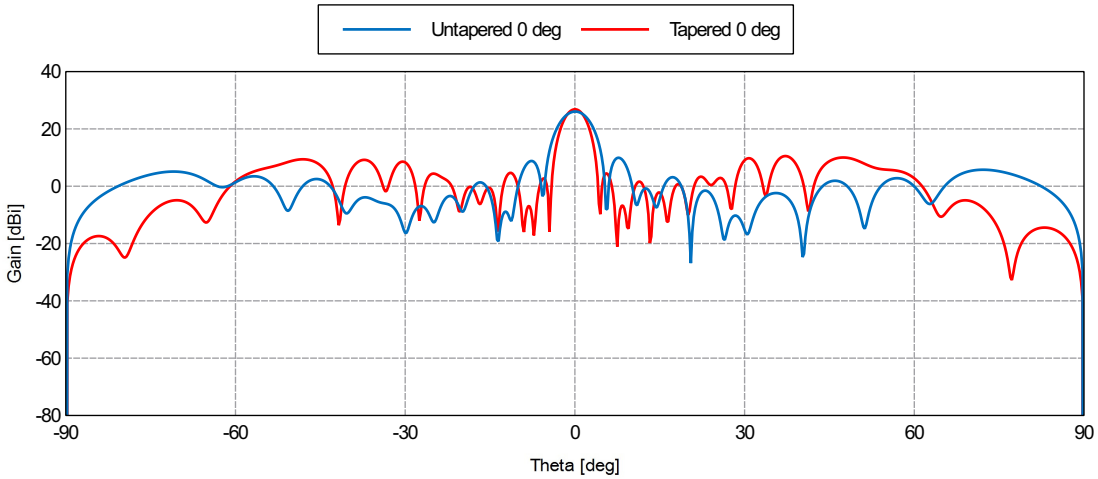

Figure 5.1: Radiation pattern of the untapered and tapered sparse array for boresight operation.

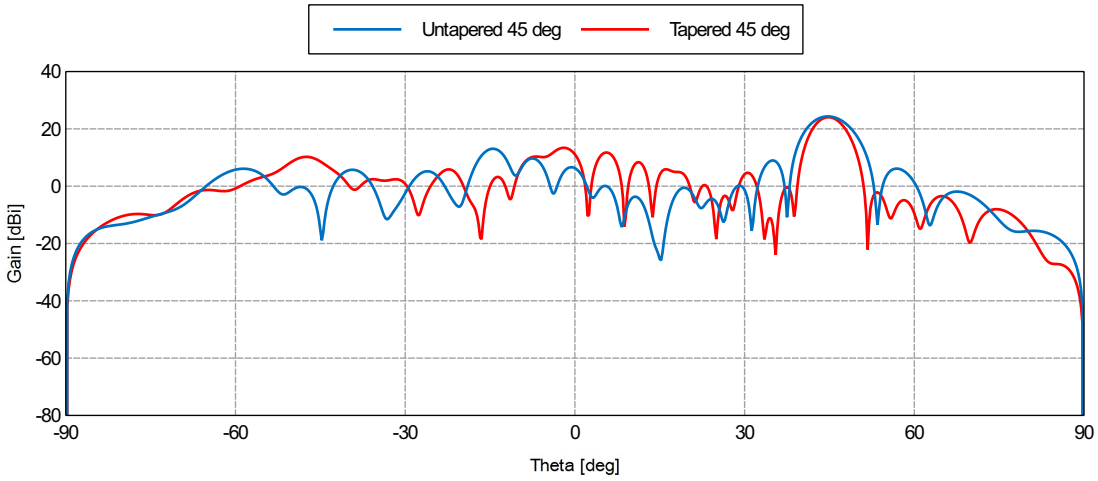

Figure 5.2: Radiation pattern of the untapered and tapered sparse array for $\theta_0 = 45°$.

Due to the scanning, the main beam has become wider since the perceived aperture has decreased. The radiation pattern shows similar characteristics as in boresight operation. However, the scanning heavily decreases the peak sidelobe level due to the individual antenna element's radiation pattern: the gain of the main beam is decreased by 3 dB and the sidelobe is shifted towards the patch's radiation pattern maximum. In this situation, the degradation of performance is most severe in the tapered array, which had its earlier peak sidelobe further away from the main beam, and now nearer to the element's maximum: its peak sidelobe level is -10.7 dB, compared to -11.3 dB for the untapered array. In fact, the high sidelobe region has 'shifted' into the visible region, nearer to the patch's radiation pattern maximum, if we address it using the analysis of Appendix B. To demonstrate the heavy burden that is placed on the array's performance when scanning the beam, for $\theta_0 = 30°$, the tapered array's peak sidelobe level is 13.2 dB and for $\theta_0 = 15°$ it is 14.8 dB.

5.2.1. COUPLING

The coupling effects are first examined from the circuitry point of view, by considering the reflection coefficient. For efficient operation, it is important that the reflection coefficient should be as low as possible (a generally accepted condition is below −10 dB). This should be achieved for every element and for every scan angle within a given frequency bandwidth.

Secondly, the simulated radiation pattern is compared to the radiation pattern gained by pattern multiplication (Equation 1.3). If coupling only plays a small role, these patterns will be in good accordance. Any discrepancy denotes the presence and severity of the coupling effects.

UNTAPERED ARRAY

Figures 5.3 to 5.6 show the reflection coefficient for a number of elements of the untapered sunflower array for different scan angles. Figure 5.3 represents patch number 1, which is the center-most element. Patch 100 is the outer-most element and is represented in Figure 5.6.

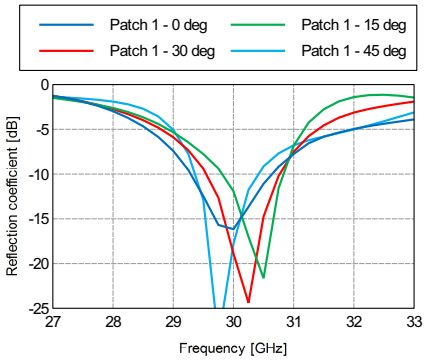

Figure 5.3: Reflection coefficient for patch 1 of the untapered sparse sunflower array.

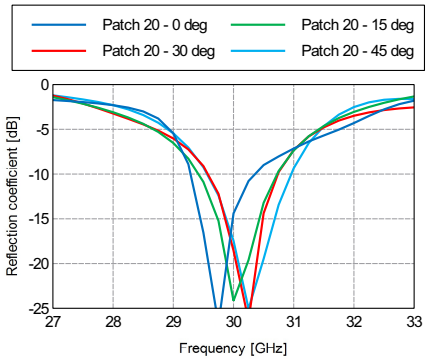

Figure 5.4: Reflection coefficient for patch 20 of the untapered sparse sunflower array.

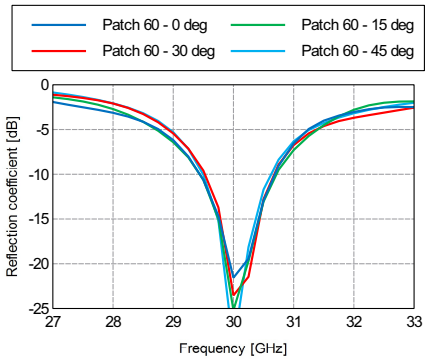

Figure 5.5: Reflection coefficient for patch 60 of the untapered sparse sunflower array.

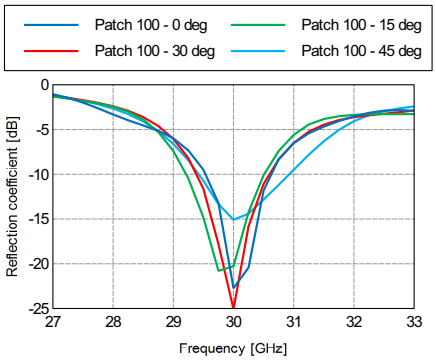

Figure 5.6: Reflection coefficient for patch 100 of the untapered sparse sunflower array.

The untapered sparse array's elements remain well matched, as their reflection coefficients remain below −10 dB at 30 GHz for every element and scan angle. For different scan angles, the center frequency shifts up to 1.7% for patch 1 and patch 20. This is not a dramatic shift and does not affect the element's performance. The value of the reflection coefficient at 30 GHz also varies, but remains below the −10 dB threshold.

Figure 5.7 shows the influence of coupling on the untapered sparse array's radiation pattern.

The dashed lines represent the radiation patterns obtained by pattern multiplication of the individual

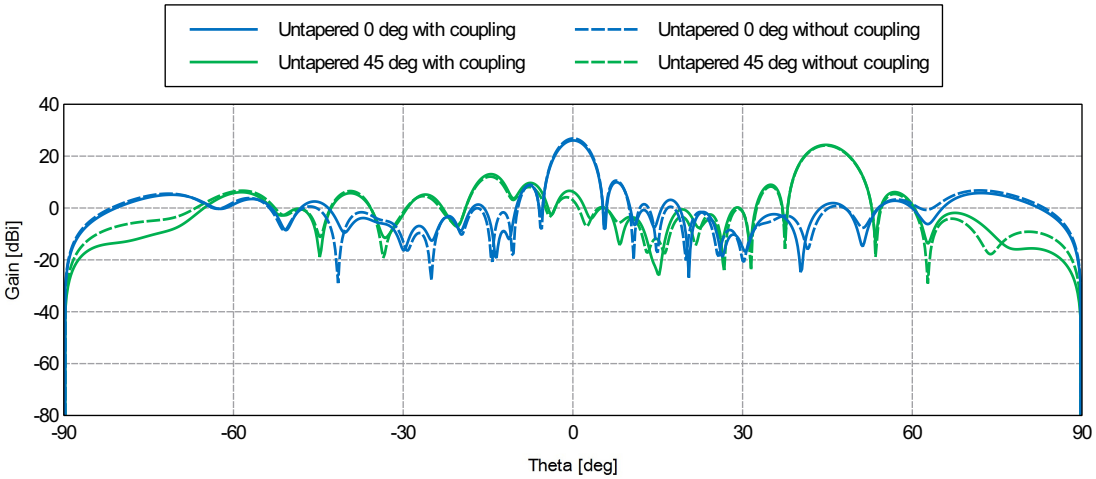

Figure 5.7: Radiation pattern of the untapered sparse array with and without coupling taken into account.

patch's radiation pattern with the array factor. It can be seen that there is little deviation between the two, which suggests that coupling effects are minor: less than 1 dB for the main beam for boresight operation and less than 0.25 dB for a maximally steered beam. The difference in relative peak sidelobe level due to coupling is also less than 1 dB for both steering angles. It can be concluded that coupling is negligible for the sparse, untapered sunflower array with 1.1λ spacing.

TAPERED ARRAY

Similarly, the reflection coefficients of elements 1, 20, 60 and 100 of the tapered array are shown in Figures 5.8, 5.9, 5.10 and 5.11.

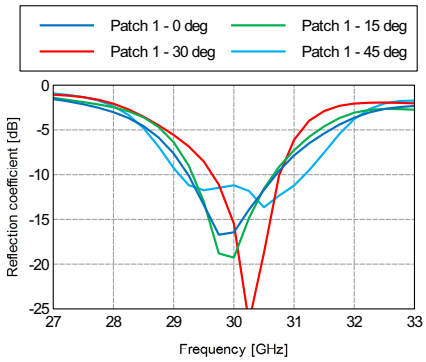

Figure 5.8: Reflection coefficient for patch 1 of the tapered sparse sunflower array.

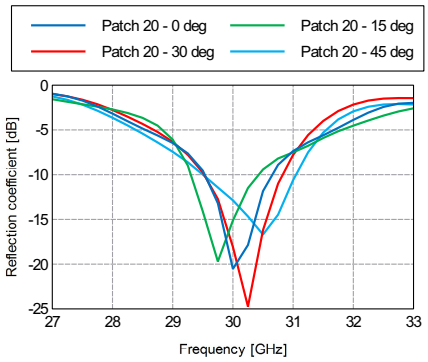

Figure 5.9: Reflection coefficient for patch 20 of the tapered sparse sunflower array.

Again, the sparsity ensures that the reflection coefficients stay below −10 dB at 30 GHz. However, compared to the plots for the untapered array, there is more variation amongst the elements. This is because of the fact that in the untapered array, all elements operate in a similar 'environment', since all are spaced equally apart from each other. With the tapered array, the element density varies, and thus the operating environment varies from element to element. Being the outermost element, patch 100 is little affected by the other patches, as Figure 5.11 shows. Patch 1, on the other hand, exhibits a considerable variation of the reflection

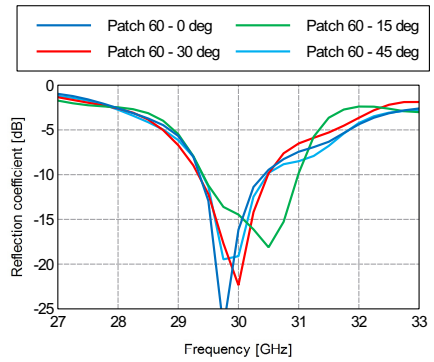

Figure 5.10: Reflection coefficient for patch 60 of the tapered sparse sunflower array.

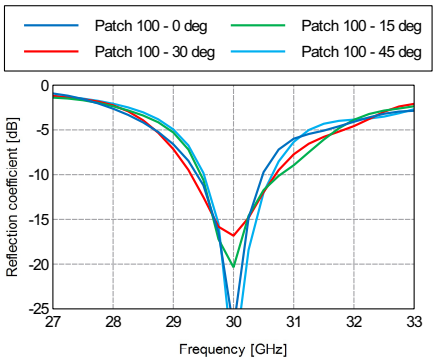

Figure 5.11: Reflection coefficient for patch 100 of the tapered sparse sunflower array.

coefficient as the beam is scanned. The absolute value of the reflection coefficient at 30 GHz varies, and the center frequency shifts by up to 2.5%, similar to patches 20 and 60. Despite these variations, the reflection coefficients stay below the −10 dB specification.

Figure 5.12 shows the radiation pattern for the tapered array with and without taking coupling into account.

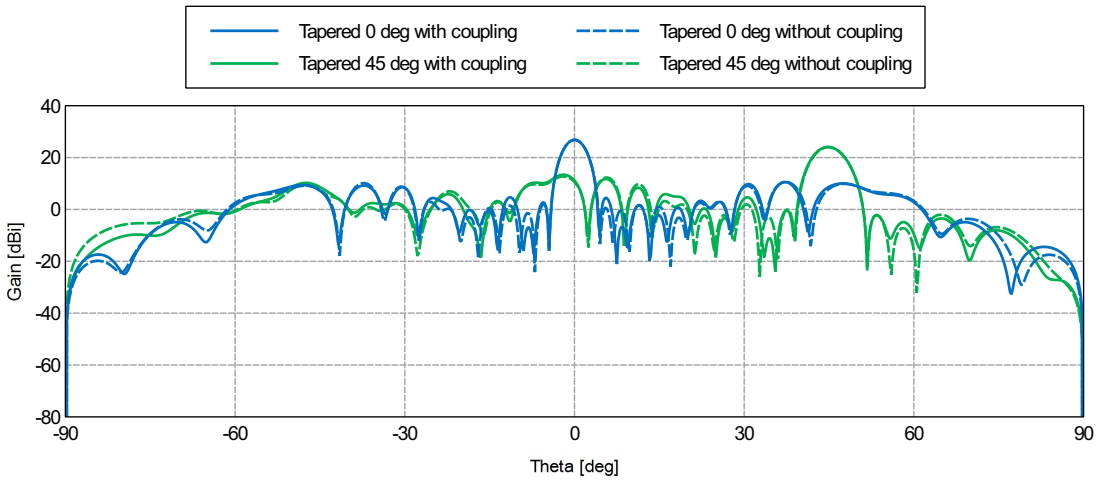

Figure 5.12: Radiation pattern of the tapered sparse array with and without coupling taken into account.

The curves barely deviate, which shows that coupling does not play a significant role. For the main beam, the difference between the curves is less than 0.1 dB for both boresight operation and when the beam is scanned to the maximum scan angle. The difference in sidelobe level by taking coupling into account is minor as well: up to 0.6 dB.

5.3. DENSE ARRAY

In this section, the same arrays will be simulated, but with 0.5λ minimum spacing between elements. The array factors of these dense arrays were more promising, as could be seen in Figure 3.13. Simulating the arrays using an electromagnetic solver will provide more realistic results. It is expected that coupling will play a more prominent role in degrading the array's performance for dense arrays.

For boresight operation, the radiation patterns are shown in Figure 5.13.

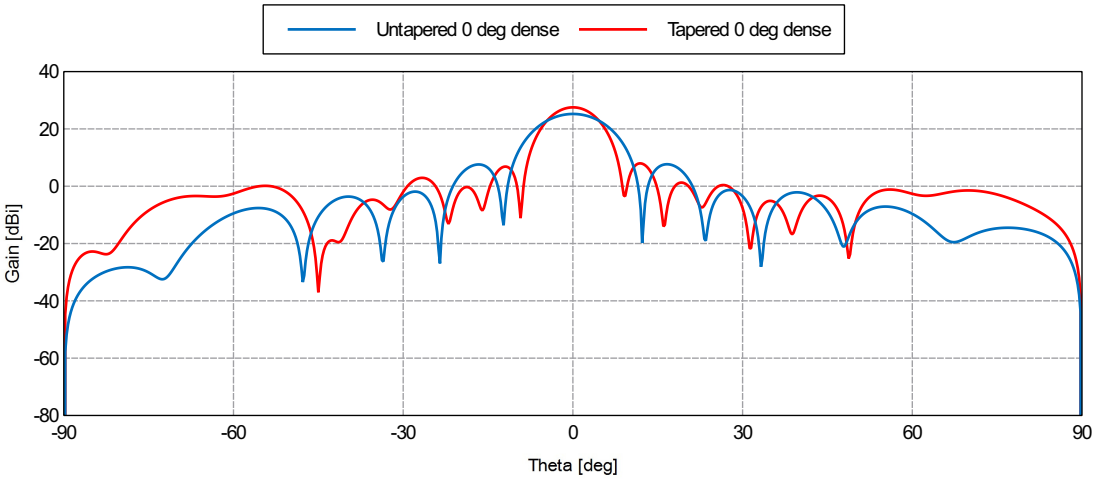

Figure 5.13: Radiation pattern of the untapered and tapered dense array for boresight operation.

From this figure it can be seen instantly that coupling plays a more significant role for these dense arrays. Firstly, the peak gain of the two arrays is visibly different, while the number of elements is identical: 25.2 dB for the untapered array versus 27.5 dB for the tapered array. Therefore, the peak gain must have been altered by coupling effects. Also, the tapered array's first sidelobes are not suppressed anymore, which is in disagreement with the tapering function and the array factor of Figure 3.13. Again, mutual coupling is the cause. Due to the difference in peak gain, however, the relative peak sidelobe level is better for the tapered array: 19.6 dB compared to 17.6 dB for the untapered array. Although the first sidelobe is not suppressed, the other sidelobes in the visible region are relatively low. For the maximum scan angle $\theta_0 = 45°$, the radiation pattern is depicted in Figure 5.14.

It can be seen that for this scan angle, the peak gain is practically the same for the tapered and untapered array, 23.4 dB and 23.6 dB, respectively. The sidelobes of the tapered array are actually higher in this situation for most of the visible region. While Figure 3.13 shows only the visible region, this region shifts when the beam is scanned to let high sidelobes enter the visible region. The end of this chapter will elaborate on this, and the conclusions that can be drawn from it.

5.3.1. COUPLING

UNTAPERED ARRAY

From the radiation pattern of Figure 5.13, it was already clear that coupling effects degrade the characteristics of the untapered dense array from the radiation pattern point of view. To find out how much the circuitry point of view is affected, the reflection coefficients of several patches are displayed in Figures 5.15 to 5.18.

It is evident that the antenna elements are no longer well matched under all operating circumstances. In almost all cases, the center frequency is shifted by up to 1.6%. As stated before, the elements behave similarly from element to element due to the similar operating environment. At 30 GHz, the varying steering angle results in a variation of the reflection coefficient of up to 10 dB, excluding the extreme dip for patch 1 at $\theta_0 = 45°$. Especially for boresight operation and scanned to $\theta_0 = 15°$, the elements' reflection patterns exceed the -10 dB mark, showing that the elements are not efficiently operated in this situation, since too much

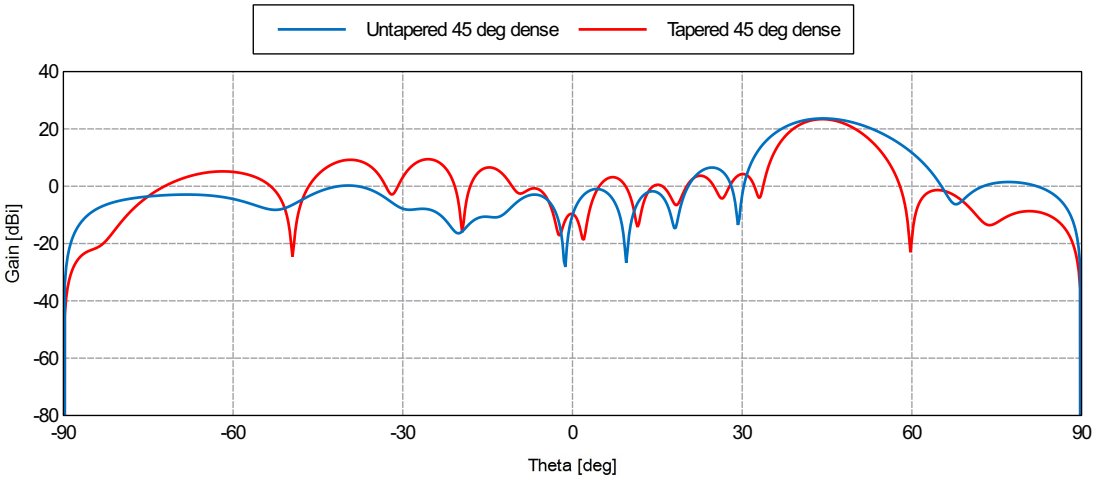

Figure 5.14: Radiation pattern of the untapered and tapered dense array for $\theta_0 = 45°$.

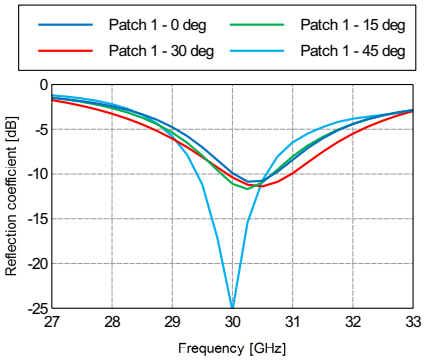

Figure 5.15: Reflection coefficient for patch 1 of the untapered dense sunflower array.

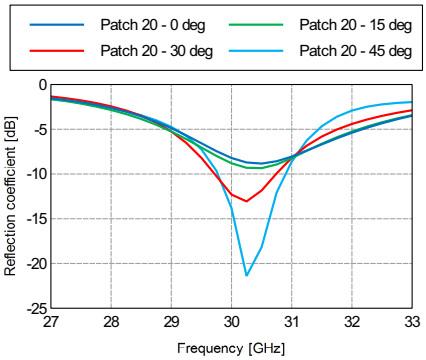

Figure 5.16: Reflection coefficient for patch 20 of the untapered dense sunflower array.

energy gets reflected to the circuitry. It is remarkable that scanning the array's main beam leads to lower reflection coefficients.

Figure 5.19 shows the radiation pattern with and without coupling taken into account for boresight and maximum scanning operation.

Over the whole visible region, coupling effects have lowered the gain. These discrepancies are more severe near the edge of the visible region. The difference is about 1.6 dB at the main beam and up to about 10 dB near the edge of the visible region. The relative sidelobe level is about 1.5 dB worse when coupling is taken into account. Altogether, it can be concluded that coupling is present, but it does not qualitatively deteriorate the radiation pattern, merely quantitatively.

TAPERED ARRAY

Next, the same analysis is applied to the tapered dense array. From Figure 5.13, it was evident that coupling plays some role, since the first sidelobe next to the main beam is no longer suppressed according to the tapering function as was the case for the sparse array. Figures 5.20 to 5.23 show the reflection coefficients of a number of the patches.

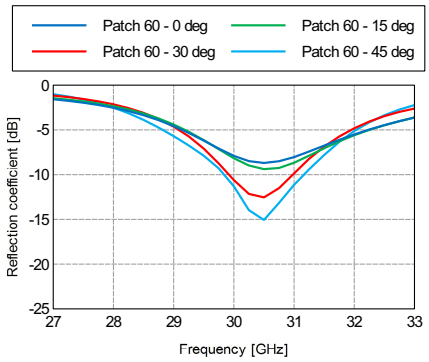

Figure 5.17: Reflection coefficient for patch 60 of the untapered dense sunflower array.

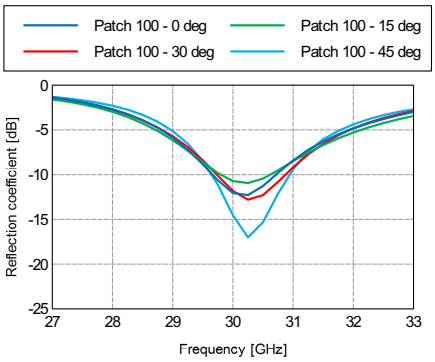

Figure 5.18: Reflection coefficient for patch 100 of the untapered dense sunflower array.

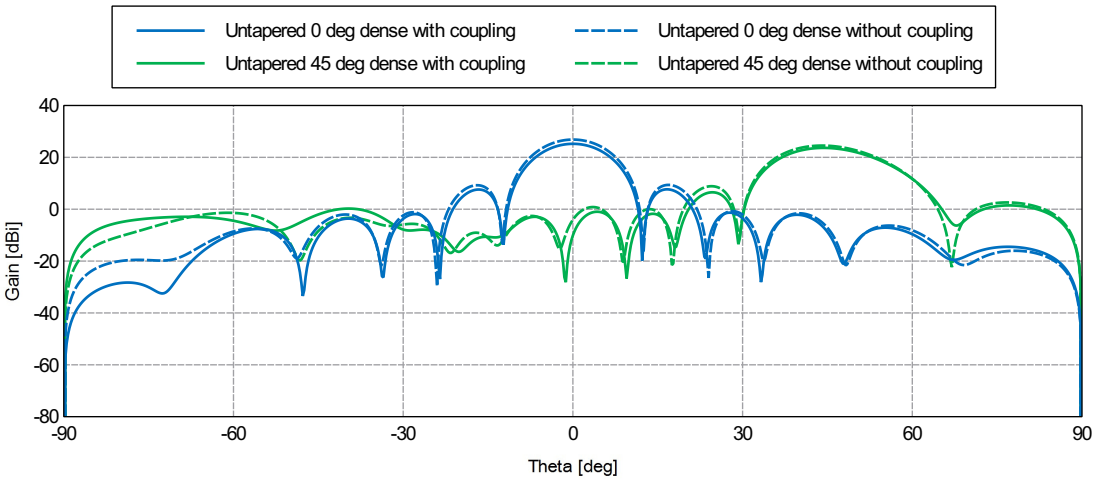

Figure 5.19: Radiation pattern of the untapered dense array with and without coupling taken into account.

From observing these figures, the antenna elements of the dense tapered array appear to be matched better than the untapered array. Although in one of the situations ($\theta_0 = 15°$ for patch 20) the reflection coefficient is higher than -10 dB at 30 GHz, the patches are well matched in all other operating conditions, despite the fact that the center frequency has shifted up to 2.5%. The absolute value of the reflection coefficient varies within 5 dB for different scan angles, but remains below -10 dB for most operating conditions. Some differences between the elements occur due to the different operating environments, and elements nearer the edge of the aperture (patch 60 and patch 100) perform slightly better. From the circuitry point of view, mutual coupling effects play a small role, even for this dense array.

To observe to what extent coupling degrades the radiating performance, the radiation pattern for boresight operation is shown with and without taking coupling into account in Figure 5.24.

The dashed line, representing the radiation pattern achieved through pattern multiplication, satisfies the desired tapering characteristics nicely: the sidelobes are neatly below the 0 dB mark, and decrease monotonically towards larger elevation angles. However, coupling effects cause the actual pattern to deviate from the tapering pattern. Especially the discrepancy of the first sidelobe is noteworthy, since this signified the difference between the tapered and untapered array factor. Due to this difference, the relative sidelobe level

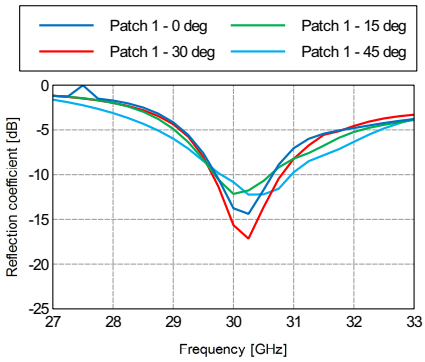

Figure 5.20: Reflection coefficient for patch 1 of the tapered dense sunflower array.

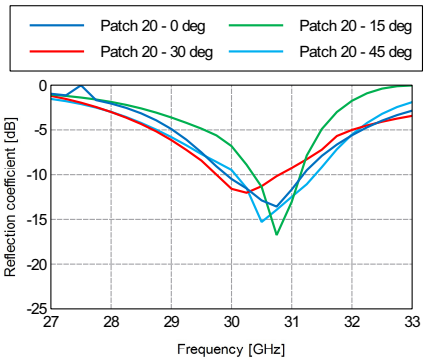

Figure 5.21: Reflection coefficient for patch 20 of the tapered dense sunflower array.

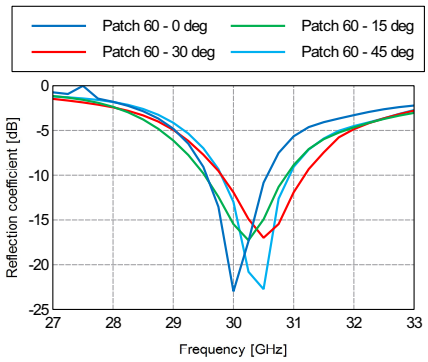

Figure 5.22: Reflection coefficient for patch 60 of the tapered dense sunflower array.

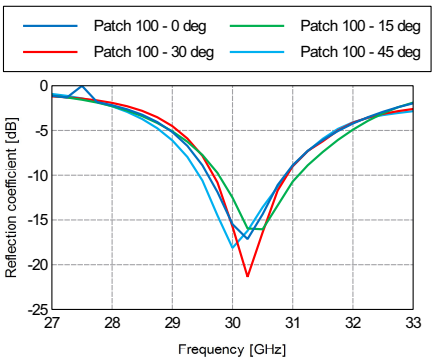

Figure 5.23: Reflection coefficient for patch 100 of the tapered dense sunflower array.

differs more than 5 dB depending on whether coupling is taken into account. At the peak gain, the difference is less than 1 dB. Further away from the main lobe, the sidelobes do behave satisfactorily. However, even this is no longer the case when scanning the beam, as can be seen in Figure 5.25, where the radiation pattern for scan angles $\theta_0 = 15°$ and $\theta_0 = 45°$ is displayed.

As described in Appendix B, scanning the beam is analogous with a shift of the visible region in the k-domain. For high scanning angles, the high sidelobe region comes into the field of view, deteriorating the peak sidelobe level from -19.6 dB for boresight operation to -19.4 dB for $\theta_0 = 15°$ and -14.0 dB for $\theta_0 = 45°$. The 0.5λ spacing was enough to ward off high sidelobes from the field of view for boresight operation, but not for scanning the beam. In Figure 3.13, only the visible region was displayed. When scanning the beam, a wider domain of the array factor is unveiled. In Figure 5.26, the same array factor in k-domain is given, but now for $0 < k_{x/y}/k < 2$.

In this figure, the visible region is denoted by the continuous red mark, and the different red line styles denote different scanning regions. For $\theta_{max} = 15°$, the high sidelobes do enter the field of view, but they are suppressed by the patch's individual radiation pattern. Larger scan angles imply that the scanning region widens, and more of the high sidelobe region enters the field of view. This can be recognized in Figure 5.25, where high sidelobes become visible as the main beam scans away from boresight. A possible solution is to further compress the topology such that the array factor in k-domain is further stretched to include a larger domain. Expanding what is the visible region now to what is the $\theta_{max} = 45°$ scanning region entails decreasing the minimum distance between elements to 0.29λ. However, coupling effects will increase and deteriorate the performance of the array further. Besides, it is questionable whether this array will be realiz-

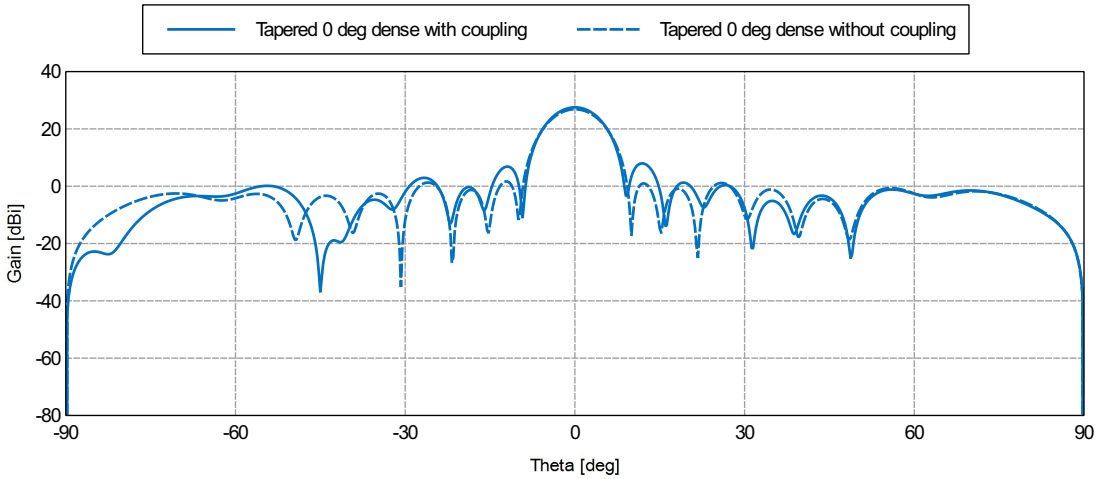

Figure 5.24: Radiation pattern of the tapered dense array with and without coupling taken into account.

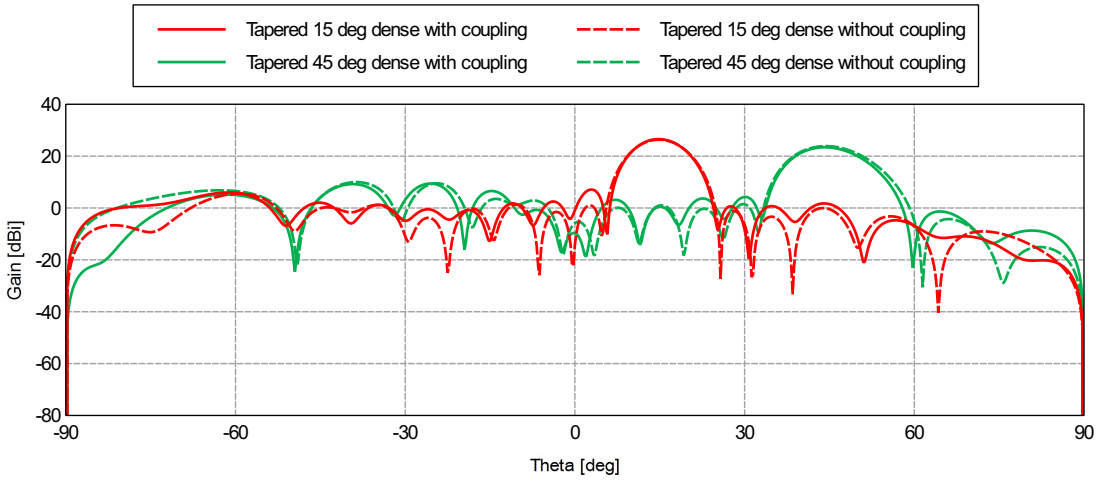

Figure 5.25: Radiation pattern of the scanned tapered dense array with and without coupling taken into account.

able due to the physical size of the elements.

5.4. CONCLUSIONS

This chapter reported on the results of the full electromagnetic wave simulations, which were executed to examine the effects of coupling.

For the sparse arrays having a minimum spacing between elements of 1.1λ, coupling effects are minor. Taking coupling into account results in a variation of the peak gain and peak sidelobe level of less than 1 dB. The reflection coefficient's variation is about 2.5%, which is also minor as it stays below the -10 dB threshold under all operating conditions. Since the foreseen base station antenna array has 1.1λ minimum spacing, it is expected that coupling effects will be negligible.

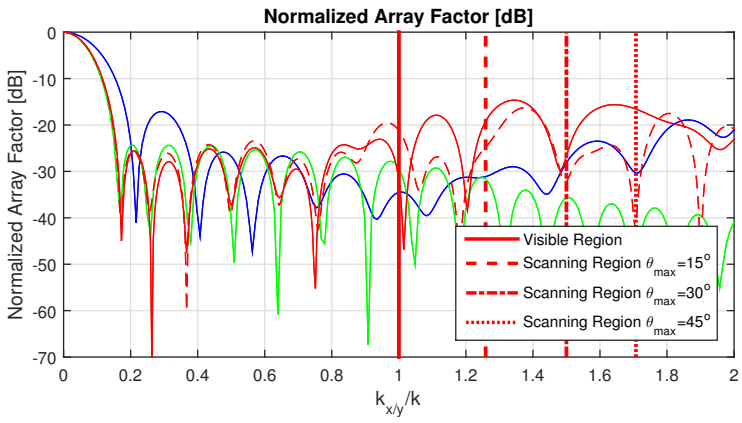

Figure 5.26: Array factor of the dense tapered array for $\phi = 0^\circ$ and $\phi = 90^\circ$.

Scanning the beam places a heavy burden on the array's performance in terms of peak sidelobe level. At boresight, the sparse tapered array's peak sidelobe level is 16.3 dB, whereas for the maximum scan angle, $\theta_0 = 45^\circ$, this has reduced to 10.7 dB. Scanning the beam up to $\theta_0 = 30^\circ$ and $\theta_0 = 15^\circ$ would result in a peak sidelobe level of 13.2 dB and 14.8 dB, respectively. This demonstrates that the scanning requirement has great consequences for the array's performance in terms of peak sidelobe level.

For dense arrays, having a minimum spacing between elements of 0.5λ, the coupling effects become more severe. Although the coupling results in a variation of the peak gain of up to 1.6 dB, the peak sidelobe level deviates by more than 5 dB and the desired tapering characteristics are not satisfied. Although the taper's characteristics are accurately approximated in the array factor, due to coupling effects they no longer hold. Moreover, for several operating conditions, the elements' reflection coefficients are above the generally accepted -10 dB threshold required for efficient operation.

This shows a fundamental trade-off of density tapering for antenna arrays: for sparse arrays the tapering approximation is valid only in a limited field of view, and for dense arrays mutual coupling effects play a significant role in degrading the array's performance such that the desired tapering properties are not satisfied.

6

Conclusions and Recommendations

6.1. Conclusions

The goal of this work was to explore the possibilities and limitations of modifying the geometrical parameters of sparse planar spiral arrays to enhance the radiation pattern. In particular, an antenna array with a minimum inter-element spacing of 1.1λ and a maximum scan angle of $\theta_{max} = 45°$ was envisioned as the next generation mobile communications generation base station antenna. To this end, both an analytical and a stochastic method have been employed. This section reports the main conclusions of these methods and their applicability to the base station antenna array.

Starting with an analytical window function as continuous current distribution, any finite element antenna array can be seen as a spatial sampling of this distribution. The sparse array's inherent undersampling property implies that the same performance cannot be achieved by such a discretized version of the continuous current distribution. It was found that this loss of information exhibits itself in the fact that the radiation pattern objective is only met in a certain field of view. The size of this region is determined by the sparseness of the array. Since this region is situated around the main lobe, the taper's properties near the main beam, such as a suppression of the first sidelobe, are satisfied even for sparse arrays.

The Fourier analysis applied in this work revealed that downscaling the whole topology to make it more dense stretches the array factor pattern in k-domain. In this domain, the Nyquist sampling rate is valid: a dense array spatially samples with $\lambda/2$ spacing so no information is lost, abstractly speaking. Therefore, the resulting array factor approximates that of the continuous distribution accurately. The downside to dense arrays is that mutual coupling effects become more pronounced.

Contrarily, the characteristics of sparse arrays having a minimum inter-element spacing of 1.1λ are barely influenced by coupling. Full electromagnetic wave simulations have shown that coupling leads to a variation of the peak gain and peak sidelobe level of less than 1 dB. The reflection coefficient remains below the -10 dB threshold under all operating conditions. Decreasing the distance between elements to 0.5λ brings about increased coupling effects that deteriorate the array's performance. Although the dense array's peak gain is only affected by up to 1.6 dB, the peak sidelobe level of the tapered dense array varies by more than 5 dB. Moreover, the common demand on the reflection coefficient of -10 dB is not satisfied for some operating conditions, preventing efficient operation. Herein lies a trade-off: a too sparse array will benefit from barely any influence of mutual coupling but the field of view where the tapering is valid is limited, while a dense array is impractical due to the deterioration of the tapering by the increased coupling effects.

Fourier theory has also established that beam steering requirements increase the region of interest in the k-domain from solely the visible region to the scanning region, which constitutes a larger circle. Such demands place a heavy burden on the performance, as the domain in which they are to be valid increases. Downscaling the topology further is limited by the physical size of the radiating elements. Moreover, coupling effects will become even more dominant.

Besides the analytical approach, a genetic algorithm has been employed in this work to stochastically obtain the optimal continuous current distribution with respect to certain characteristics. Simply approximating this optimal continuous distribution leads to the array factor following the continuous optimum's radiation pattern to a certain extent.

To see whether the optimum continuous current distribution is also the optimum current distribution

for finite element arrays, arrays with varying number of elements have been optimized independently. This revealed that for dense arrays, the optima are in agreement. Decreasing the number of elements makes the optimum deviate slightly, but effectively the performance is similar to that of the array based on the continuous optimum distribution, even for very sparse arrays. Therefore, it has been shown that when optimizing a planar array, a single optimization of the continuous current distribution is sufficient to obtain the practically optimum distribution for finite element arrays as well.

In particular, the effectiveness of the proposed density tapering methods for the envisioned base station antenna array application is limited. Although a hard requirement on the sidelobes was not set, applying density tapering to a spiral array with a minimum spacing between elements of 1.1λ and scanning the beam up to $\theta_{max} = 45°$, as proposed in Chapter 1, barely improves the performance compared to an untapered array. Full electromagnetic wave simulations have shown that a $\bar{n} = 10, SLL = -25$ dB Taylor tapered array's radiation pattern's sidelobes are only lower near the main beam. For boresight operation, the sparse tapered array's peak sidelobe level is -16.3 dB, compared to -16.1 dB for the untapered array. The main difference lies in the location of this peak: the untapered array's peak sidelobe is the first sidelobe. Depending on the application, the location of the peak sidelobe may be of interest, and a well-considered decision can be made. For the base station antenna, such a criterion is not yet defined, and depends on system level specifications.

Relaxed system level specifications on the maximum scan angle may also improve the array's performance in terms of peak sidelobe level. For the current $\theta_{max} = 45°$, the peak sidelobe level is -10.7 dB, compared to -13.2 dB for $\theta_{max} = 30°$ and -14.8 dB for $\theta_{max} = 15°$.

To conclude, density tapering may not improve the absolute performance of a sparse array in terms of peak sidelobe level, but may be useful if the region of interest is concentrated near the main beam. In the base station application, this may be the case when interfering users are positioned near the designated user. I hope that the observations and explored limitations prove insightful in the further development of the next generation mobile communications base station antenna array.

6.2. NOVELTY

The novelty presented in this work lies mainly in the exploration of the limitations of density tapering for sparse arrays with a substantial scan angle. In the literature, density tapering is either applied to dense arrays or to sparse arrays with a sole interest in the region near boresight, such as in satellite communications.

Furthermore, expressing the current density as a polynomial that is the subject of optimization is also novel. Amongst the many ways researchers have reduced the optimization problem, this is not a method I came across. This method has led to the conclusion that an aperture only needs to be optimized once, and the resulting current distribution is optimum for finite element arrays as well, which is to my knowledge also novel.

6.3. RECOMMENDATIONS

To complement the contents of this thesis, full electromagnetic wave simulations may be done for the optimized array topologies. In addition, other patch antennas may be evaluated. Even though this probably does not offer new insights, it adds to the completeness of this work.

Furthermore, this work has focused solely on modifying the radial coordinates of the spiral array's elements to limit the scope. Further work may attempt to improve the performance by using another base topology, although I believe that the above conclusions apply to sparse arrays in general.

Further degrees of freedom are to be obtained if the phase of the elements' excitations is modified as well. As a downside, some peak gain will be given up since there is no longer perfect constructive interference. It should be investigated whether the sidelobes can be suppressed to such a degree that it also compensates for the peak gain loss. The phase can be either optimized stochastically, or an analytical method could be applied. A marginal amplitude deviation may also aid to this end.

As stated with regard to the continuous optimization statements, further research should be done with different requirements to establish whether the proposed conclusion holds in general.

A

Window Function

A.1. Linear Window

A tapering function is a window that is designed to fulfill certain characteristics when Fourier transformed. Examples include the Chebyshev window function, which achieves a certain specified constant sidelobe level, and the Taylor window function, which achieves a certain specified constant sidelobe level for the first $\bar{n}$ sidelobes with monotonically decreasing sidelobes afterwards. In Figure A.1, an example is given of a Taylor distribution with $\bar{n} = 4, SLL = -35$ dB. The left figure shows the time-domain window function, and the right figure shows the Fourier-transformed frequency domain function.

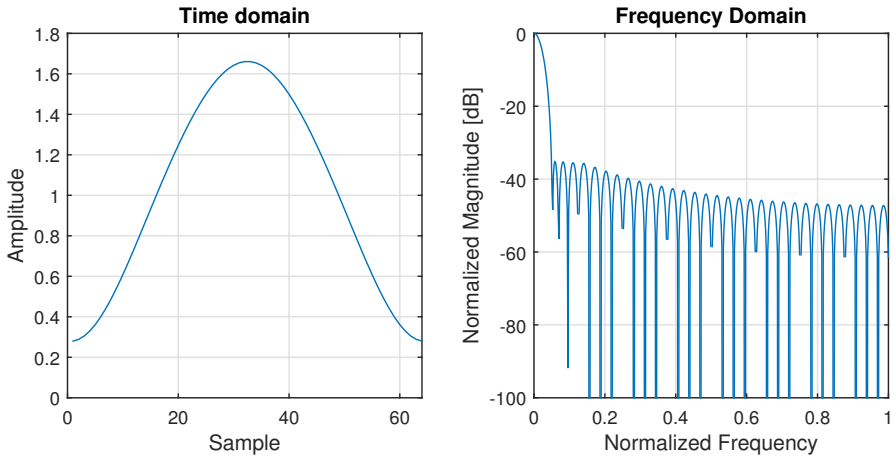

Figure A.1: Example of a Taylor distribution with $\bar{n} = 4, SLL = -35$ dB.

The sidelobe level can be specified as any desired value. However, it should be noted that this comes at a cost. The energy which is removed by suppressing the sidelobes adds to the main lobe, making it wider. Most window functions exchange certain sidelobe characteristics at the cost of a wider main beam.

Window functions can be used as a desired current distribution, of which the characteristics will then be exhibited in the radiation pattern. In antenna arrays, this current distribution can be approximated by means of tapering, either by amplitude or by density. When using amplitude tapering, the regular array's antenna elements' amplitudes are altered to match the amplitude of the window function at that position. When using density tapering, the elements' positions are modified such that the element density, and thus the current density, approximates that of the specified window function. Because realistic antenna arrays consist of a finite number of elements, the continuous window function is sampled in space. As will be seen, well-known sampling theories apply such as the Nyquist sampling criterion.

A.2. CIRCULAR WINDOW

Due to shadowing effects, linear window functions cannot be applied to a circular aperture directly. From an arbitrary observation point, the aperture's current distribution is projected onto the axis of the direction of observation. If the linear window is to be used, the characteristic properties of this projected distribution would no longer be valid due to the different distribution. Therefore, an adapted window should be used in circular apertures, that achieves the same characteristics when looking from any angle, by applying this distribution symmetrically as a function of the radius.

A circular window is derived by Taylor [89] that satisfies the same properties as the linear Taylor window: $\bar{n}$ equal sidelobes of specified sidelobe level with monotonically decreasing sidelobes beyond. The current distribution of this circularly symmetric window is given as a function of the normalized radius $\tilde{r} = r/R_{ap}$, the number of sidelobes to be of the specified sidelobe level $\bar{n}$ and the specified sidelobe level SLL by

$$A(\tilde{r}) = \sum_{m=0}^{\bar{n}-1} \frac{2F(\mu_m, B, \bar{n})}{[J_0(\pi\mu_m)]^2\pi^2} J_0(\pi\mu_m\tilde{r}) \tag{A.1}$$

where

$$F(\mu_m, B, \bar{n}) = \begin{cases} 1 & m = 0 \\ -J_0(\pi\mu_m) \dfrac{\prod_{n=1}^{\bar{n}-1} 1 - \dfrac{\mu_m^2}{\sigma[B^2 + (n-\frac{1}{2})^2]}}{\prod_{\substack{n=1 \\ n\neq m}}^{\bar{n}-1} 1 - \dfrac{\mu_m^2}{\mu_n^2}} & 0 < m < \bar{n} \\ 0 & m \geq \bar{n} \end{cases} \tag{A.2}$$

in which μ_n is the nth solution to $J_1(\pi\mu_n) = 0$ where $J_\alpha(x)$ is the Bessel function of the first kind for integer order α, B is a parameter related to the specified sidelobe level by $SLL_{linear} = \cosh(\pi B)$ and σ is the so-called dilation factor, given by

$$\sigma = \frac{\mu_{\bar{n}}}{\sqrt{B^2 + (\bar{n} - 1/2)^2}} \tag{A.3}$$

To observe the differences between the circular and the linear window, Figures A.2 to A.10 show several window functions for a number of $\bar{n}$ and SLL.

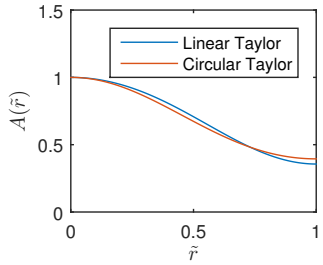

Figure A.2: $\bar{n} = 3, SLL = -25$ dB

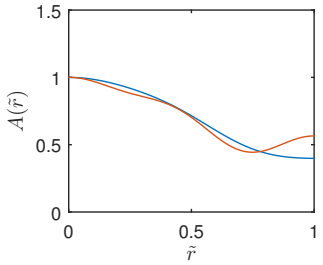

Figure A.3: $\bar{n} = 5, SLL = -25$ dB

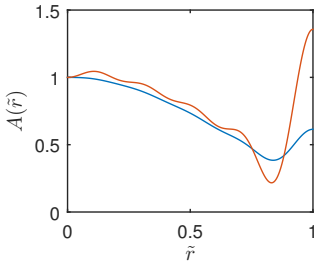

Figure A.4: $\bar{n} = 10, SLL = -25$ dB

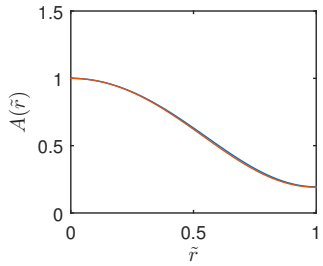

Figure A.5: $\bar{n} = 3, SLL = -35$ dB

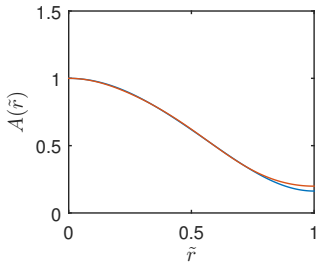

Figure A.6: $\bar{n} = 5, SLL = -35$ dB

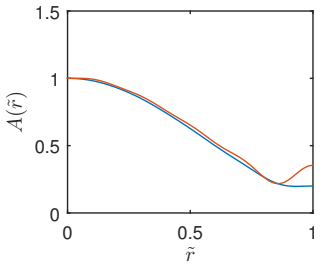

Figure A.7: $\bar{n} = 10, SLL = -35$ dB

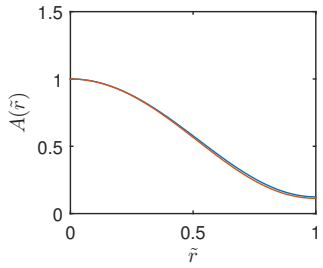

Figure A.8: $\bar{n} = 3, SLL = -45$ dB

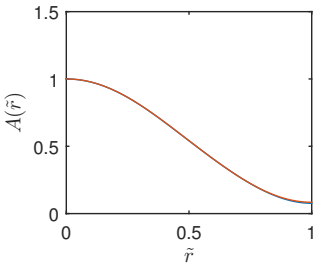

Figure A.9: $\bar{n} = 5, SLL = -45$ dB

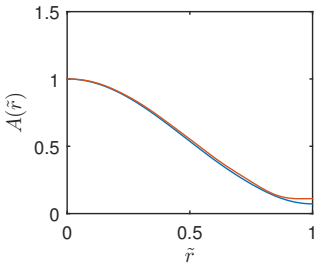

Figure A.10: $\bar{n} = 10, SLL = -45$ dB

It can be seen that the main differences appear for high $\bar{n}$ and relatively low SLL. Due to shadowing, the difference between the circular and linear window appear mainly near the maximum of the radius. Near this edge of the aperture, the function, and thus the desired current density, increases considerably. Using a realistic continuous aperture, a high current at the edge is difficult to achieve because of the aperture's boundary conditions. Fortunately, when approximating this continuous current distribution by means of density tapering, this is rather convenient, since the high radius allows us to achieve a high element density while keeping the distance between its neighbours high.

B

Analysis Method

Evaluating the performance of an array for each steering angle (θ_0, ϕ_0) in the scanning region would require many calculations of the array factor. There is, however, an approach that makes this analysis much quicker. This appendix will explain the method and the insights that can be obtained from it.

First, the two-dimensional spatial Fourier transform of the current distribution is taken:

$$\hat{j}(k_x, k_y) = \int\int j(x,y) e^{-j(k_x x + k_y y)} dx dy \tag{B.1}$$

Since at this stage, the current distribution is given by the elements' complex excitation $w_n = a_n e^{j\varphi_n}$ at discrete locations x_n, y_n ($z_n = 0$), this integral becomes a sum:

$$\hat{j}(k_x, k_y) = \sum_{n=1}^{N} w_n e^{-j(k_x x_n + k_y y_n)} = \sum_{n=1}^{N} w_n e^{-j\boldsymbol{k}\cdot\boldsymbol{r}_n} \tag{B.2}$$

which is another way of writing Equation 1.2. In equation B.2, $\boldsymbol{k} = k\left[\sin(\theta)\cos(\phi)\hat{\boldsymbol{x}} + \sin(\theta)\sin(\phi)\hat{\boldsymbol{y}}\right]$ where $k = \frac{2\pi}{\lambda}$ is the wave number. The fact that we are able to use the well-known Fourier transform allows us to exploit its mathematical properties, as will become clear later in this chapter.

In this k-domain, the visible region can be calculated from the trigonometric functions for real angles in the definition of $\boldsymbol{k}$:

$$-1 \leq \sin(\cdot) \leq 1 \tag{B.3}$$

$$-1 \leq \cos(\cdot) \leq 1 \tag{B.4}$$

such that

$$\sqrt{k_x^2 + k_y^2} \leq k \tag{B.5}$$

which constitutes a circle in the $k_x k_y$-plane with radius k. The above expression of the array factor in the wavenumber domain also allows us to observe the array factor behaviour beyond the visible region, when choosing k_x or k_y such that $\sqrt{k_x^2 + k_y^2} > k$. The usefulness of this will be explained later in this appendix. A visual representation of the k-domain in relation to the ordinary coordinate system is given in Figure B.1.

Now, let us analyse some array factors. Firstly, a square grid regular array is analysed with $N = 100$ elements and $d_x = d_y = d = \lambda/2$ inter-element spacing, the topology of which can be seen in Figure B.2. The circle in Figure B.3 marks the visible region and it is evident that no grating lobes appear in it. An increase in the inter-element spacing will cause grating lobes to appear in the visible region. This effect is illustrated in Figure B.5, where the array factor is shown for the same 100-element array but with $d = \lambda$.

The increase of inter-element spacing has 'compressed' the array factor in k-domain. Further increasing d will lead to more grating lobes entering the visible region. This corresponds to our knowledge of Fourier analysis, where a fine (dense) signal in time (space) domain transforms to a wide signal in frequency domain and vice versa. In these figures, we can also recognize the well-known property that the larger the antenna array aperture, the narrower its main beam, similar as long time pulses relate to low frequency bandwidths

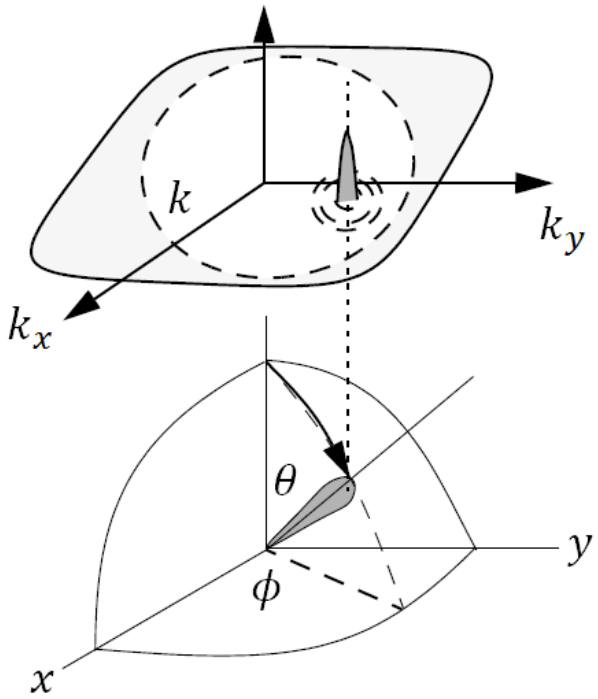

Figure B.1: Visual representation of the array factor in k-domain [90].

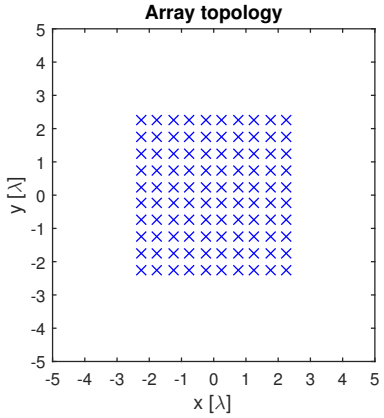

Figure B.2: Topology of the dense regular array.

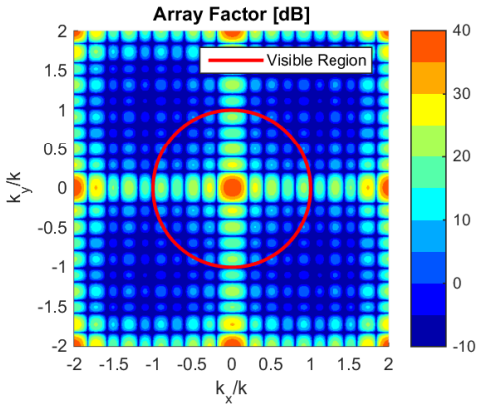

Figure B.3: Array factor of the regular array with $d = \lambda/2$.

in time-frequency transforms. The sidelobes of the pattern correspond to the frequency harmonics of an equivalent time waveform and rapid transitions in time lead to high levels of harmonics in the frequency domain [3]. Similarly, step transitions in the current distribution produces high sidelobes, while tapering the edges reduces sidelobes.

When steering the main beam, a phase shift φ_n is applied to each element such that all signals add coherently in a certain direction $\boldsymbol{k_0} = k\left[\sin(\theta_0)\cos(\phi_0)\hat{\boldsymbol{x}} + \sin(\theta_0)\sin(\phi_0)\hat{\boldsymbol{y}}\right]$:

$$w_n = a_n e^{j\varphi_n} = a_n e^{-j\boldsymbol{k_0}\cdot\boldsymbol{r_n}} \tag{B.6}$$

Filling this in the array factor equation gives

$$AF(k_x, k_y) = \sum_{n=1}^{N} w_n e^{-j\boldsymbol{k}\cdot\boldsymbol{r}_n} = \sum_{n=1}^{N} a_n e^{-j\boldsymbol{k_0}\cdot\boldsymbol{r_n}} e^{-j\boldsymbol{k}\cdot\boldsymbol{r}_n} = \sum_{n=1}^{N} a_n e^{-j(\boldsymbol{k}+\boldsymbol{k_0})\cdot\boldsymbol{r}_n} \tag{B.7}$$

which shows that applying phase-shifts to the elements' excitations to steer the beam in a certain $\boldsymbol{k_0}$ gives a translation in k-domain, which also corresponds to our knowledge of Fourier analysis. The translation in

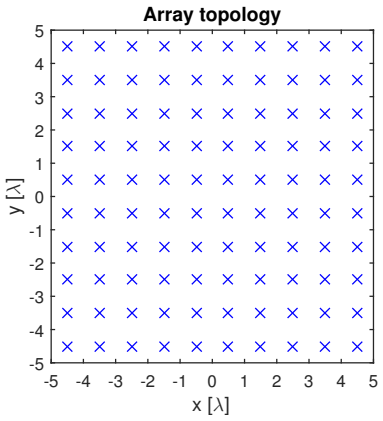

Figure B.4: Topology of the sparse regular array.

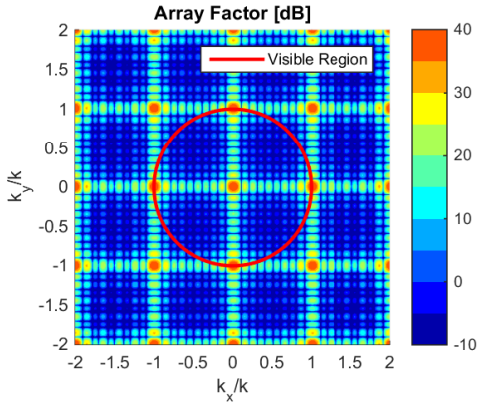

Figure B.5: Array factor of the regular array with $d = \lambda$.

the k-domain can be seen as a shift of the visible region. Figure B.7 shows the array factor of the previously shown regular array with $d = \lambda$ spacing, when the beam is steered to $\theta_0 = 45°$. In the figure, the shifted visible region for $\phi_0 = 0$ is shown by the continuous red line. Furthermore, this region can be shifted for each ϕ_0 to constitute a so-called scanning region, which contains all possible steering angles for θ_{max}. The scanning region is the circle given by

$$\sqrt{k_x^2 + k_y^2} \leq k(1 + \sin(\theta_{max}) \tag{B.8}$$

In Figure B.7, this scanning region is denoted for $\theta_{max} = 45°$, according to the specification from Section 1.1.

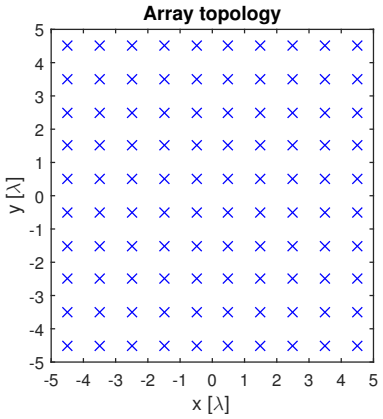

Figure B.6: Topology of the sparse regular array.

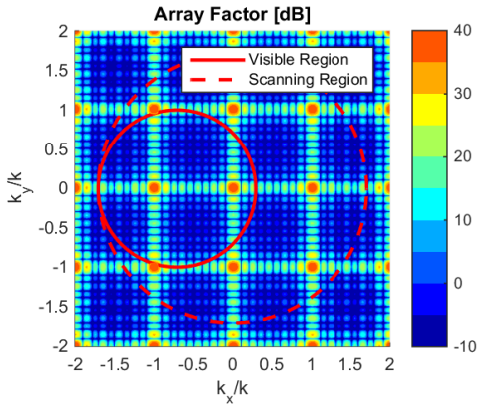

Figure B.7: Array factor of the regular array with $d = \lambda$, with a steered beam.

These tools allow us to evaluate the performance of the array's array factor in the whole scanning region with only one calculation. Also, the effects of scaling the topology can be predicted with this method, which is a great advantage.

Up to now we have only looked at array factors of regular arrays, where grating lobes will be present. For the sunflower topology with parameters $s = 1.1\lambda, N = 100$ the array factor is shown in Figure B.9.

It can be seen that even far beyond the visible region, no grating lobes are present. The sidelobe energy is distributed over the rest of the region. The peak sidelobe level is determined by the yellow ring which is just within the visible region when looking at boresight. Besides this ring, the first sidelobe around the main beam is the next highest sidelobe. Beyond the ring, the sidelobe level is quite constant for a large region. Although there are no grating lobes, the significance of the ring's sidelobe level is illustrated in the following calculation.

The relative sidelobe level of the array factor in the ring is about 8.5 dB, at $k_x/k \approx 0.87$, which corresponds to $\theta \approx 60°$. To illustrate the consequences for operation with a realistic antenna element, consider an elemen-

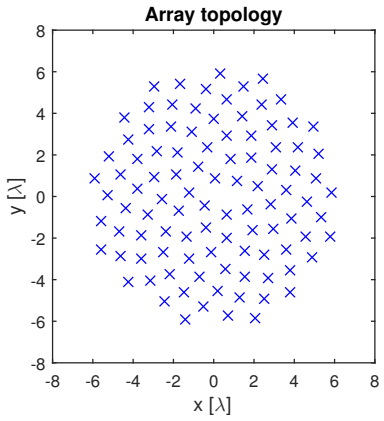

Figure B.8: Topology of the sunflower array.

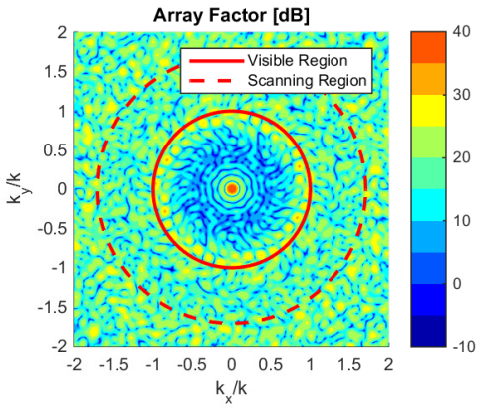

Figure B.9: Array factor of the sunflower array.

tary circular patch antenna with a 90° beamwidth such that at $\theta = 45°$ ($0° < \phi < 360°$), its gain is -3 dB relative to the boresight gain. Such an element is required in order to achieve $\theta_{max} = 45°$ scanning performance with -3 dB scan loss. At $\theta = 60°$, its gain is about -5 dB relative to the boresight gain.

For boresight operation, the patch antenna's maximum is aligned with the array factor's maximum. The relative sidelobe level will therefore be $-8.5 - 5 = -13.5$ dB. For operation at the edge of the scanning region ($\theta_0 = 45°$), the main beam will be -3 dB relative to the main beam in boresight operation due to the patch's radiation pattern. The peak sidelobe level (the ring) of the array factor will be shifted to $\frac{k_x}{k} = \sin(45°) - \sin(60°) = \frac{1}{2}\sqrt{2} - \frac{1}{2}\sqrt{3} = -0.16$ which corresponds to $\theta = -9.1°$. This is the calculation of the beamsteering translation in k-domain. At this angle, the patch's gain is 0.1 dB below its boresight gain, so the sidelobe level is $-8.5 - 0.1 = -8.6$ dB. Since the main beam gain is reduced by 3 dB due to the scan loss, the relative sidelobe level is only -5.6 dB.

This preliminary calculation shows that the scanning of the array's beam places a heavy burden on the peak sidelobe level performance, and for large scan angles the sidelobe level in the ring plays a significant role.

C

GENETIC ALGORITHM

This appendix will explain the genetic algorithm step by step. This optimization algorithm is based on the theory of evolution: parameters are encoded as binary sequences called genes which make up chromosomes. A population of chromosomes undergoes natural selection, mates and mutates to arrive at the optimal solution.

Firstly, the N_{par} parameters p_n which are to be optimized are encoded in binary sequences. An array of these quantized parameters, called genes, makes up a chromosome, which can be seen as one realization of the variable parameters:

$$\text{chromosome} = [p_1, p_2, \ldots, p_{N_{par}}] \tag{C.1}$$

The continuous parameters p_n need to be encoded into a binary sequence of N_{pbit} bits. Naturally, a higher choice of N_{pbit} results in a finer resolution. This is one of the parameters that need to be defined in the initial stage. The quantized version of p_n is given by

$$q_n = \sum_{m=1}^{N_{pbit}} b_n[m] 2^{1-m} Q \tag{C.2}$$

where b_n is the binary sequence associated with q_n (and thus p_n) and Q is the largest quantization level which is half the largest-possible value of q_n.

The total population consists of many chromosomes. For each chromosome a cost function is calculated, which has the chromosome's genes as its input and a single scalar value as the output:

$$\text{cost} = f([p_1, p_2, \ldots, p_{N_{par}}]) \tag{C.3}$$

With the cost of each chromosome calculated, they can be sorted to undergo 'natural selection'. The best chromosomes survive and mate to form the next generation population. This process repeats itself until it converges or reaches a pre-specified goal.

In Figure C.1, a flowchart is displayed that outlines the process. The remainder of this appendix will describe the steps involved in this flowchart.

- The initial step is to define all associated functions and variables such as the cost function and the variables to be optimized. While this may seem a mere formality, the art and effectiveness of the optimization algorithm depends on choosing the initial conditions appropriately. The genetic algorithm itself has some parameters such as the size of the population and the mutation chance that need to be specified as well.
- The initial population is created by randomly generating M chromosomes.
- The binary chromosomes are then decoded to decipher the associated parameter values.
- For each chromosome, the associated cost is calculated by using the cost function.

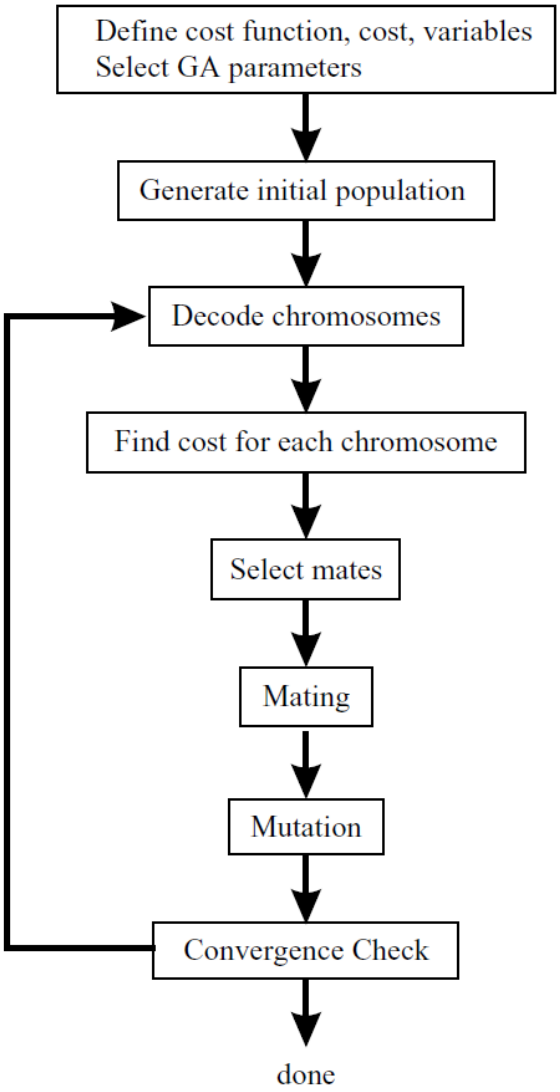

Figure C.1: Flowchart of a genetic algorithm [71].

- The chromosomes are then sorted by their costs from best to worst. The best half are kept, while the others are discarded. The number of chromosomes to keep can be chosen by the designer.
- The leftover chromosomes mate, that is, produce offspring that consist of pieces of the leftover chromosomes. Below, this is illustrated for two offspring that inherit parts of two parents [70]. In this example, the chromosome consists of 12 bits and the crossover point is at the fifth bit. The crossover point can be chosen freely.

$$\text{parent \#1} = \overbrace{10101}\underline{0010101}$$
$$\text{parent \#2} = \overline{11100}\underbrace{1100101}$$

$$\text{offspring \#1} = \overbrace{10101}\underbrace{1100101}$$

$$\text{offspring \#2} = \overline{11100}\underline{0010101}$$

- After the mating, the mutation takes place. All bits in the population have a chance of mutation, usually in the order of a few percent, that they are flipped from 1 to 0 or vice versa. This random disturbance

of the algorithm allows it to search the total search space and prevents getting stuck in local optima. To speed up convergence, the chromosome with the best cost can be made immune to mutation.

- With the previous step, the population of the next generation is complete and the process is ready for the next iteration. A check for convergence is executed to assess whether the algorithm has converged and the optimum solution is found. Alternatively, a maximum number of iterations can be set and the algorithm is stopped when that number is reached.

The general structure of a genetic algorithm is straightforward and easy to implement. However, the difficulty lies in aptly choosing the parameters which are to be optimized and the cost function on which to optimize.

BIBLIOGRAPHY

[1] Ericsson, *Mobility report february 2016,* (2016).

[2] C. A. Balanis, *Antenna Theory* (Wiley & Sons, 2005).

[3] T. A. Milligan, *Modern Antenna Design* (Wiley & Sons, 2005).

[4] P. Rocca, G. Oliveri, R. J. Mailloux, and A. Massa, *Unconventional phased array architectures and design methodologies - a review,* Proceedings of the IEEE **104**, 544 (2016).

[5] R. C. Hansen, *Microwave Scanning Antennas* (Academic Press, 1964).

[6] R. J. Mailloux, *Phased Array Antenna Handbook*, 2nd ed. (Artech House, Boston, 2005).

[7] A. Ishimaru and Y. Chen, *Thinning and broadbanding antenna arrays by unequal spacings,* IEEE Transactions on Antennas and Propagation **13**, 34 (1965).

[8] G. R. Lockwood, P.-C. Li, M. O'Donnell, and F. S. Foster, *Optimizing the radiation pattern of sparse periodic linear arrays,* IEEE Transactions on Ultrasonics, Ferroelectrics, and Frequency Control **43**, 7 (1996).

[9] G. R. Lookwood and F. S. Foster, *Optimizing the radiation pattern of sparse periodic two-dimensional arrays,* IEEE Transactions on Ultrasonics, Ferroelectrics, and Frequency Control **43**, 15 (1996).

[10] D. G. Leeper, *Isophoric arrays-massively thinned phased arrays with well-controlled sidelobes,* IEEE Transactions on Antennas and Propagation **47**, 1825 (1999).

[11] G. Oliveri, M. Donelli, and A. Massa, *Linear array thinning exploiting almost difference sets,* IEEE Transactions on Antennas and Propagation **57**, 3800 (2009).

[12] G. Oliveri, P. Rocca, and A. Massa, *Analytic techniques for the design of non-regular arrays,* in *Phased Array Systems and Technology (ARRAY), 2010 IEEE International Symposium on* (2010) pp. 737–739.

[13] R. Willey, *Space tapering of linear and planar arrays,* IRE Transactions on Antennas and Propagation **10**, 369 (1962).

[14] M. Skolnik, J. Sherman, and F. Ogg, *Statistically designed density-tapered arrays,* IEEE Transactions on Antennas and Propagation **12**, 408 (1964).

[15] B. Steinberg, *Comparison between the peak sidelobe of the random array and algorithmically designed aperiodic arrays,* IEEE Transactions on Antennas and Propagation **21**, 366 (1973).

[16] R. L. Haupt, *Thinned arrays using genetic algorithms,* IEEE Transactions on Antennas and Propagation **42**, 993 (1994).

[17] C. I. Coman, I. E. Lager, and L. P. Ligthart, *Design considerations in sparse array antennas,* in *Radar Conference, 2006. EuRAD 2006. 3rd European* (2006) pp. 72–75.

[18] S. Hebib, N. Raveu, and H. Aubert, *Cantor spiral array for the design of thinned arrays,* IEEE Antennas and Wireless Propagation Letters **5**, 104 (2006).

[19] D. S. Goshi and T. Itoh, *Sparse array optimization with directive elements for millimeter-wave application,* in *Millimeter Waves, 2008. GSMM 2008. Global Symposium on* (2008) pp. 138–141.

[20] G. Oliveri, L. Manica, and A. Massa, *On the impact of mutual coupling effects on the psl performances of ads thinned arrays,* Progress In Electromagnetics Research B **17**, 293 (2009).

[21] Z. Bayraktar, M. Komurcu, J. A. Bossard, and D. H. Werner, *The wind driven optimization technique and its application in electromagnetics,* IEEE Transactions on Antennas and Propagation **61**, 2745 (2013).

[22] W. P. M. N. Keizer, *Synthesis of thinned planar circular and square arrays using density tapering,* IEEE Transactions on Antennas and Propagation **62**, 1555 (2014).

[23] H. Unz, *Linear arrays with arbitrarily distributed elements,* IRE Transactions on Antennas and Propagation **8**, 222 (1960).

[24] A. Maffett, *Array factors with nonuniform spacing parameter,* IRE Transactions on Antennas and Propagation **10**, 131 (1962).

[25] B. Steinberg, *The peak sidelobe of the phased array having randomly located elements,* IEEE Transactions on Antennas and Propagation **20**, 129 (1972).

[26] D. H. Werner, W. Kuhirun, and P. L. Werner, *The peano-gosper fractal array,* IEEE Transactions on Antennas and Propagation **51**, 2063 (2003).

[27] V. Pierro, V. Galdi, G. Castaldi, I. M. Pinto, and L. B. Felsen, *Radiation properties of planar antenna arrays based on certain categories of aperiodic tilings,* IEEE Transactions on Antennas and Propagation **53**, 635 (2005).

[28] Y. Kim and D. L. Jaggard, *The fractal random array,* Proceedings of the IEEE **74**, 1278 (1986).

[29] K. C. Kerby and J. T. Bernhard, *Sidelobe level and wideband behavior of arrays of random subarrays,* IEEE Transactions on Antennas and Propagation **54**, 2253 (2006).

[30] T. A. Milligan, *Space-tapered circular (ring) array,* IEEE Antennas and Propagation Magazine **46**, 70 (2004).

[31] O. M. Bucci, T. Isernia, A. F. Morabito, S. Perna, and D. Pinchera, *Aperiodic arrays for space applications: An effective strategy for the overall design,* in *Antennas and Propagation, 2009. EuCAP 2009. 3rd European Conference on* (2009) pp. 2031–2035.

[32] O. M. Bucci, T. Isernia, A. F. Morabito, S. Perna, and D. Pinchera, *Density and element-size tapering for the design of arrays with a reduced number of control points and high efficiency,* in *Antennas and Propagation (EuCAP), 2010 Proceedings of the Fourth European Conference on* (2010) pp. 1–4.

[33] O. M. Bucci and S. Perna, *A deterministic two dimensional density taper approach for fast design of uniform amplitude pencil beams arrays,* IEEE Transactions on Antennas and Propagation **59**, 2852 (2011).

[34] Y. Jiang and S. Zhang, *An innovative strategy for synthesis of uniformly weighted circular aperture antenna array based on the weighting density method,* IEEE Antennas and Wireless Propagation Letters **12**, 725 (2013).

[35] P. Angeletti, G. Toso, and G. Ruggerini, *Array antennas with jointly optimized elements positions and dimensions part ii: Planar circular arrays,* IEEE Transactions on Antennas and Propagation **62**, 1627 (2014).

[36] O. M. Bucci, T. Isernia, S. Perna, and D. Pinchera, *Isophoric sparse arrays ensuring global coverage in satellite communications,* IEEE Transactions on Antennas and Propagation **62**, 1607 (2014).

[37] C. Bencivenni, M. V. Ivashina, R. Maaskant, and J. Wettergren, *Design of maximally sparse antenna arrays in the presence of mutual coupling,* IEEE Antennas and Wireless Propagation Letters **14**, 159 (2015).

[38] J. Fondevila-Gómez, A. A. Salas-Sánchez, J. A. Rodríguez-González, and F. J. Ares-Pena, *Density-tapered planar arrays for multibeam and shaped beam coverage in satellite communications,* in *2015 9th European Conference on Antennas and Propagation (EuCAP)* (2015) pp. 1–5.

[39] O. M. Bucci and D. Pinchera, *A generalized hybrid approach for the synthesis of uniform amplitude pencil beam ring-arrays,* IEEE Transactions on Antennas and Propagation **60**, 174 (2012).

[40] D. H. Werner, W. Kuhirun, and P. L. Werner, *Fractile arrays: a new class of broadband tiled arrays with fractal boundaries,* in *Antennas and Propagation Society International Symposium, 2004. IEEE*, Vol. 1 (2004) pp. 563–566 Vol.1.

[41] J. N. Bogard, D. H. Werner, and P. L. Werner, *Comparison of the peano–gosper fractile array and the regular hexagonal array,* Microwave and Optical Technology Letters **43**, 524 (2004).

[42] J. N. Bogard and D. H. Werner, *Optimization of peano-gosper fractile arrays using genetic algorithms to reduce grating lobes during scanning,* in *Radar Conference, 2005 IEEE International* (2005) pp. 905–909.

[43] T. G. Spence and D. H. Werner, *Generalized space-filling gosper curves and their application to the design of wideband modular planar antenna arrays,* IEEE Transactions on Antennas and Propagation **58**, 3931 (2010).

[44] T. G. Spence, D. H. Werner, and J. N. Carvajal, *Modular broadband phased-arrays based on a nonuniform distribution of elements along the peano-gosper space-filling curve,* IEEE Transactions on Antennas and Propagation **58**, 600 (2010).

[45] R. Penrose, *The role of aesthetics in pure and applied mathematical research,* Bull. Inst. Math. Appl **10**, 266 (1974).

[46] B. Grünbaum and G. C. Shepard, *Tilings and Patterns* (Freeman, New York, 1987).

[47] T. G. Spence and D. H. Werner, *Design of broadband planar arrays based on the optimization of aperiodic tilings,* IEEE Transactions on Antennas and Propagation **56**, 76 (2008).

[48] T. Isernia, M. D'Urso, and O. M. Bucci, *A simple idea for an effective sub-arraying of large planar sources,* IEEE Antennas and Wireless Propagation Letters **8**, 169 (2009).

[49] R. Mailloux, S. Santarelli, T. Roberts, and D. Luu, *Irregular polyomino-shaped subarrays for space-based active arrays,* International Journal of Antennas and Propagation **2009** (2009), 10.1155/2009/956524.

[50] M. D. Gregory, D. H. Werner, and P. L. Werner, *Nature-inspired techniques for the synthesis of aperiodic ultra-wideband phased arrays,* in *Phased Array Systems and Technology (ARRAY), 2010 IEEE International Symposium on* (2010) pp. 707–712.

[51] M. D'Urso, M. G. Labate, A. Buonanno, and P. Vinetti, *Effective beam forming networks for large arbitrary array of antennas,* IEEE Transactions on Antennas and Propagation **60**, 5129 (2012).

[52] P. Rocca, R. J. Mailloux, and G. Toso, *Ga-based optimization of irregular subarray layouts for wideband phased arrays design,* IEEE Antennas and Wireless Propagation Letters **14**, 131 (2015).

[53] T. G. Spence and D. H. Werner, *Multiobjective optimization in the design of broadband arrays based on aperiodic tilings,* in *Antennas and Propagation Society International Symposium, 2008. AP-S 2008. IEEE* (2008) pp. 1–4.

[54] T. Spence and D. Werner, *Full-wave mutual coupling analysis of wideband arrays based on aperiodic tilings,* in *Antennas and Propagation Society International Symposium, 2009. APSURSI '09. IEEE* (2009) pp. 1–4.

[55] M. Gregory, F. Namin, and D. Werner, *Exploiting rotational symmetry for the design of ultra-wideband planar phased array layouts,* IEEE Transactions on Antennas and Propagation **61**, 176 (2013).

[56] J. L. Schwartz and B. D. Steinberg, *Ultrasparse, ultrawideband arrays,* IEEE Transactions on Ultrasonics, Ferroelectrics, and Frequency Control **45**, 376 (1998).

[57] D. Boeringer, *Phased array including a logarithmic spiral lattice of uniformly spaced radiating and receiving elements,* (2002), uS Patent 6,433,754.

[58] O. Martínez-Graullera, C. J. Martín, G. Godoy, and L. G. Ullate, *2d array design based on fermat spiral for ultrasound imaging,* Ultrasonics **50**, 280 (2010).

[59] M. C. Viganó, *Sunflower Array Antenna for Multi-Beam Satellite Applications*, Ph.D. thesis, Delft University of Technology (2011).

[60] A. Ramalli and P. Tortoli, *256-element density-tapered spiral matrices for ultrasound phased imaging,* in *Ultrasonics Symposium (IUS), 2014 IEEE International* (2014) pp. 2087–2090.

[61] L. H. Gabrielli and H. E. Hernandez-Figueroa, *Aperiodic antenna array for secondary lobe suppression,* IEEE Photonics Technology Letters **28**, 209 (2016).

[62] G. Toso, P. Angeletti, and C. Mangenot, *A comparison of density and amplitude tapering for transmit active arrays,* in *Antennas and Propagation, 2009. EuCAP 2009. 3rd European Conference on* (2009) pp. 840–843.

[63] R. Harrington, *Sidelobe reduction by nonuniform element spacing,* IRE Transactions on Antennas and Propagation **9**, 187 (1961).

[64] M. Andreasen, *Linear arrays with variable interelement spacings,* IRE Transactions on Antennas and Propagation **10**, 137 (1962).

[65] Y. Lo and S. Lee, *A study of space-tapered arrays,* IEEE Transactions on Antennas and Propagation **14**, 22 (1966).

[66] P. D. Anderson, M. A. Ingram, and V. K. Tripp, *A new density tapering method based on radial warping,* IEEE Transactions on Antennas and Propagation **46**, 1763 (1998).

[67] S. S. Kuo, G. P. Junker, T. K. Wu, and C. H. Chen, *A density taper technique for low side lobe applications of hex array antennas,* in *Phased Array Systems and Technology, 2000. Proceedings. 2000 IEEE International Conference on* (2000) pp. 493–496.

[68] S. Suárez, G. León, M. Arrebola, L. F. Herrán, and F. Las-Heras, *Linear aperiodic array of microstrip patch antennas with grating lobes reduction,* in *Antennas and Propagation Society International Symposium (APSURSI), 2012 IEEE* (2012) pp. 1–2.

[69] M. Mitchell, *An Introduction to Genetic Algorithms* (MIT Press, Cambridge, MA, USA, 1996).

[70] R. L. Haupt, *An introduction to genetic algorithms for electromagnetics,* IEEE Antennas and Propagation Magazine **37**, 7 (1995).

[71] R. L. Haupt and S. E. Haupt, *Practical Genetic Algorithms with CD-ROM* (Wiley-Interscience, 2004).

[72] M. Bray, D. Werner, D. Boeringer, and D. Machuga, *Optimization of thinned aperiodic linear phased arrays using genetic algorithms to reduce grating lobes during scanning,* IEEE Transactions on Antennas and Propagation **50**, 1732 (2002).

[73] K. Chen, X. Yun, Z. He, and C. Han, *Synthesis of sparse planar arrays using modified real genetic algorithm,* IEEE Transactions on Antennas and Propagation **55**, 1067 (2007).

[74] J. Galejs, *Minimization of sidelobes in space tapered linear arrays,* IEEE Transactions on Antennas and Propagation **12**, 497 (1964).

[75] J. Perini and M. Idselis, *Note on antenna pattern synthesis using numerical iterative methods,* IEEE Transactions on Antennas and Propagation **19**, 284 (1971).

[76] R. Redlich, *Iterative least-squares synthesis of nonuniformly spaced linear arrays,* IEEE Transactions on Antennas and Propagation **21**, 106 (1973).

[77] T. Clavier, N. Razavi-Ghods, F. Glineur, D. Gonzalez-Ovejero, E. de Lera Acedo, C. Craeye, and P. Alexander, *A global-local synthesis approach for large non-regular arrays,* IEEE Transactions on Antennas and Propagation **62**, 1596 (2014).

[78] V. Murino, A. Trucco, and C. Regazzoni, *Synthesis of unequally spaced arrays by simulated annealing,* IEEE Transactions on Signal Processing **44**, 119 (1996).

[79] J. Kennedy and R. Eberhart, *Particle swarm optimization,* in *Neural Networks, 1995. Proceedings., IEEE International Conference on*, Vol. 4 (1995) pp. 1942–1948 vol.4.

[80] D. W. Boeringer and D. H. Werner, *Particle swarm optimization versus genetic algorithms for phased array synthesis,* IEEE Transactions on Antennas and Propagation **52**, 771 (2004).

[81] R. Storn and K. Price, *Minimizing the real functions of the icec'96 contest by differential evolution,* in *Evolutionary Computation, 1996., Proceedings of IEEE International Conference on* (1996) pp. 842–844.

[82] P. Rocca, G. Oliveri, and A. Massa, *Differential evolution as applied to electromagnetics,* IEEE Antennas and Propagation Magazine **53**, 38 (2011).

[83] C. Rocha-Alicano, D. Covarrubias-Rosales, C. Brizuela-Rodriguez, and M. Panduro-Mendoza, *Differential evolution algorithm applied to sidelobe level reduction on a planar array,* {AEU} - International Journal of Electronics and Communications **61**, 286 (2007).

[84] J. Sahalos, *Orthogonal Methods for Array Synthesis: Theory and the ORAMA Computer Tool* (Wiley, 2006).

[85] T. N. Kaifas and J. N. Sahalos, *On the geometry synthesis of uniformy excited conformal arrays by the orthogonal method,* in *Antennas and Propagation, 2007. EuCAP 2007. The Second European Conference on* (2007) pp. 1–6.

[86] T. N. Kaifas, D. G. Babas, G. S. Miaris, K. Siakavara, E. E. Vafiadis, and J. N. Sahalos, *Aperiodic array layout optimization by the constraint relaxation approach,* IEEE Transactions on Antennas and Propagation **60**, 148 (2012).

[87] M. D. Gregory, Z. Bayraktar, and D. H. Werner, *Fast optimization of electromagnetic design problems using the covariance matrix adaptation evolutionary strategy,* IEEE Transactions on Antennas and Propagation **59**, 1275 (2011).

[88] B. V. Ha, R. E. Zich, M. Mussetta, and P. Pirinoli, *Synthesis of sparse planar array using modified bayesian optimization algorithm,* in *Electromagnetics in Advanced Applications (ICEAA), 2013 International Conference on* (2013) pp. 1541–1543.

[89] T. Taylor, *Design of circular apertures for narrow beamwidth and low sidelobes,* IRE Transactions on Antennas and Propagation **8**, 17 (1960).

[90] B. R. Mahafza, *MATLAB Simulations for Radar Systems Design* (Chapman & Hall/CRC CRC Press LLC, 2004).